

# MeltwaterBench: Deep learning for spatiotemporal downscaling of surface meltwater

Björn Lütjens<sup>1,†</sup>, Patrick Alexander<sup>2</sup>, Raf Antwerpen<sup>2</sup>,  
Til Widmann<sup>3</sup>, Guido Cervone<sup>4</sup>, Marco Tedesco<sup>2</sup>

<sup>1</sup>Department of Earth, Atmospheric, and Planetary Sciences, Massachusetts Institute of Technology

<sup>2</sup>Lamont Doherty Earth Observatory, Columbia University

<sup>3</sup>Massachusetts Institute of Technology

<sup>4</sup>Institute for Computational and Data Sciences, Pennsylvania State University

## Key Points:

- We create 100m resolution daily maps of surface meltwater over the Helheim Glacier, Greenland from 2017 to 2023 using deep learning
- Downscaling regional climate model projections using satellite data increases accuracy wrt. our chosen targets from 83% to 95%
- We publish an open-source benchmark for assessing deep learning methods on spatiotemporal gap-filling

---

Corresponding author: Björn Lütjens, † current affiliation at IBM Research,  
lutjens[at]mit.edu

## Abstract

The Greenland ice sheet is melting at an accelerated rate due to processes that are not fully understood and hard to measure. The distribution of surface meltwater can help understand these processes and is observable through remote sensing, but current maps of meltwater face a trade-off: They are either high-resolution in time or space, but not both. We develop a deep learning model that creates gridded surface meltwater maps at daily 100m resolution by fusing data streams from remote sensing observations and physics-based models. In particular, we spatiotemporally downscale regional climate model (RCM) outputs using synthetic aperture radar (SAR), passive microwave (PMW), and a digital elevation model (DEM) over the Helheim Glacier in Eastern Greenland from 2017-2023. Using SAR-derived meltwater as “ground truth”, we show that a deep learning-based method that fuses all data streams is over 10 percentage points more accurate over our study area than existing non deep learning-based approaches that only rely on a regional climate model (83% vs. 95% Acc.) or passive microwave observations (72% vs. 95% Acc.). Alternatively, creating a gridded product through a running window calculation with SAR data underestimates extreme melt events, but also achieves notable accuracy (90%) and does not rely on deep learning. We evaluate standard deep learning methods (UNet and DeepLabv3+), and publish our spatiotemporally aligned dataset as a benchmark, *MeltwaterBench*, for intercomparisons with more complex data-driven downscaling methods. The code and data are available at [github.com/blutjens/hrmelt](https://github.com/blutjens/hrmelt).

## Plain language summary

Understanding why the Greenland ice sheet has been melting faster is challenging due to the difficulty of observing the underlying processes. An important observable indicator is surface meltwater, which is water that forms on top of or within the first meters of the ice sheet. The highest resolution information on surface meltwater can be derived from satellites with a synthetic aperture radar (SAR) instrument, but the resulting data is hard to use due to temporal gaps from the satellites’ flight paths. During such temporal gaps an extreme meltwater event that can produce billions of tons of meltwater within a single day could have occurred. To simplify the use of surface meltwater data, we propose a deep learning method that creates regularly-spaced, daily, high-resolution maps of surface meltwater. The deep learning model does so by fusing the information from SAR with other satellite data and physics-based simulations that are available on a daily basis. We show that surface meltwater maps from our deep learning model are significantly more accurate than currently used maps. And, to encourage the development of more complex models we publish our data as a benchmark dataset.

## 1 Introduction

The Greenland ice sheet (GrIS) is melting at its fastest rate in 12,000 years (Briner et al., 2020) and has contributed to approximately a quarter (4cm) of the past-century sea level rise (Fox-Kemper et al., 2021). Projections of how such contribution will change in the future vary greatly (5-33cm by 2100) which is partially due to regional climate model uncertainty in ice mass loss processes and feedbacks (Aschwanden et al., 2019). Remote sensing instruments can help quantify ice mass loss processes, for example, by observing surface meltwater and linking it to atmospheric drivers as well as ice mass loss (Mattingly et al., 2018, 2023). But, current observations of surface meltwater from different satellite instruments face shortcomings with respect to either spatial resolution, temporal coverage, or physical observability. We propose a deep learning-based downscaling method that can fuse remote sensing and modeled data into a daily high-resolution (100m) surface meltwater product to fill these data gaps and, eventually reduce uncertainties in the future GrIS sea level rise contribution.

The primary spaceborne instruments for observing surface meltwater - optical, microwave, and radar - can miss localized and rapid ice mass loss processes, such as coastal melt events (Noël et al., 2017): Optical remote sensing can detect surface water, but sub-surface water to a lesser extent, and is frequently obscured by cloud cover in Eastern Greenland (Miles et al., 2017; Häkkinen et al., 2014). Passive microwave (PMW) observations occur daily and can penetrate clouds, but have a spatial resolution of 3.25–25km (Ashcraft & Long, 2006; Colosio et al., 2020). Coarsely-resolved daily information is also available from in-situ point observations (Fausto et al., 2021) or regional climate model (RCM) reanalyses, such as the 5km Modèle Atmosphérique Régional v3.14 (MAR; Grailet et al., 2024). Yet, coarse data can miss topographic features that lead to enhanced melting (Noël et al., 2016), is error-prone in coastal areas due to single pixels covering both land and ocean, and can miss important hydrological features such as crevasses, meltwater rivers, or lakes (van de Berg et al., 2020; Noël et al., 2016; McMillan et al., 2016). Very high-resolution information on surface meltwater can be retrieved from cloud-penetrating radar, e.g., Sentinel-1 Synthetic Aperture Radar (SAR) since 2017 at 10m, but the revisit time of 2-12 days can miss the onset of extreme melt events that can produce billions of tons of meltwater within a single day, as detailed in Section 2.3. The low-frequency revisit also hinders a better understanding of the effect of rapid rainfall events, atmospheric rivers, or strong foehn winds on local supraglacial hydrology (van den Broeke et al., 2023; Bailey & Hubbard, 2025; Mattingly et al., 2023). In summary, the coarse spatial or temporal resolution of data sources represents a barrier to understanding melting processes.

A few downscaling methods exist for merging datasets in space and time, but deep learning has not yet been evaluated as a method for downscaling surface meltwater in Greenland. Instead, lower order functional fits have been used to produce daily 1km (Noël et al., 2016) or 100m (Tedesco et al., 2023) surface meltwater maps in Greenland by combining RCM output and reanalyses with a static digital elevation model (DEM). Despite being valuable for understanding meltwater processes, efforts like this mostly focus on local interpolation approaches, such as linear regression, random forest, or gradient boosting fits in local ( $\sim 3 \times 3$ px) neighborhoods. This approach enhances spatial resolution, but does not correct for larger-scale spatial biases in the input data streams (Noël et al., 2016; Tedesco et al., 2023). Deep learning methods, such as convolutional neural networks (CNNs), can correct large-scale biases and have been proposed for downscaling surface meltwater (de Roda Husman et al., 2024a, 2024b). Most similar to our work, de Roda Husman et al. (2024a) created 12-hourly 500m maps of surface meltwater fraction over Antarctica by fusing remote sensing data (SAR and PMW) with a UNet, which is a common CNN-based encoder-decoder architecture (Ronneberger et al., 2015). In comparison, our study focuses on Greenland and incorporates RCM simulations.

Downscaling spatiotemporal data is common across Earth system modeling with deep learning being seen as a promising technique (Mardani et al., 2025). Benchmarks that define an accessible dataset, metrics, and strong baselines are crucial to understanding if deep learning is achieving meaningful progress (Lütjens et al., 2025; Rasp et al., 2020). Benchmarks related to downscaling focus on super-resolution of single-image (Agustsson & Timofte, 2017; Karras et al., 2018; Kurinchi-Vendhan et al., 2021), multi-image (Wolters et al., 2023), or video data (C. Liu & Sun, 2014). But, most datasets in super-resolution use input and target imagery of the same modality and do not contain large-scale biases, i.e., the regional average of high-resolution target pixels equals the value of the corresponding low-resolution input pixel (Harder et al., 2023). In comparison, downscaling requires the correction of large-scale biases and translation across modalities, such as mapping PMW and DEM information onto surface meltwater. To the best of our knowledge, only two benchmarks exist for evaluating deep learning methods for downscaling: X. Chen et al. (2022) evaluates methods on downscaling global to regional precipitation reanalysis over the Eastern US, which does not capture the issue of translation across modalities. Langguth et al. (2024) released a dataset for downscaling atmospheric variables over the Alps, but it is missing baseline methods.

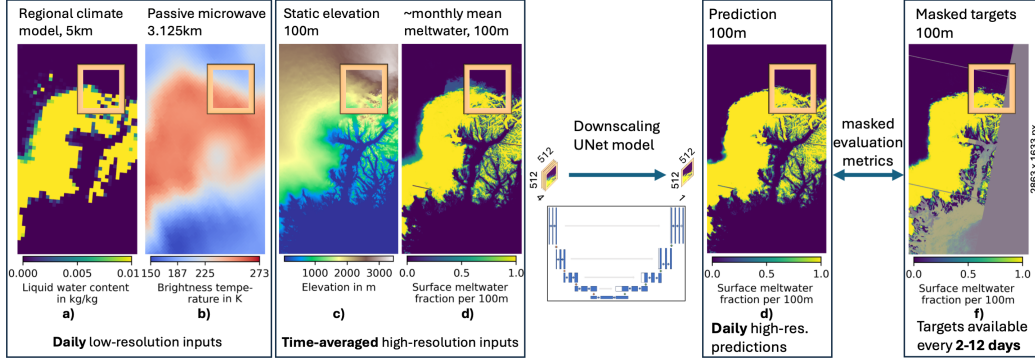


Figure 1: **Overview.** Our benchmark, MeltwaterBench, poses a downscaling task, which is to predict a high-resolution Sentinel-1 SAR-derived map of surface meltwater fraction (f). These meltwater observations are only available every 2-12 days and are partially masked (f; gray area), due to the Sentinel-1 retrieval paths. The benchmark evaluates which machine learning method can most accurately predict meltwater maps, given low-resolution data from a regional climate model (a; MAR) and passive microwave observations (b; PMW). The available inputs also include a digital elevation model (c; DEM), a running mean of meltwater observations (d; time-interpolated SAR), and optional auxiliary atmospheric variables and optical satellite observations (not shown; see Table A1), which are not used in our baseline UNet. The images display June 24, 2018.

We propose a benchmark dataset, metrics, and baselines for evaluating deep learning methods on spatiotemporal downscaling of RCM-simulated surface meltwater over a study area surrounding the Helheim Glacier in Eastern Greenland. For this study area, we derived 100m surface meltwater fraction for all available Sen-1 SAR observations using a well-validated threshold-based approach (Ashcraft & Long, 2006). With the surface meltwater targets, we created a machine learning (ML)-ready dataset from 2017-2023 with spatiotemporally-aligned inputs from the 5km MAR regional climate model reanalysis, PMW, and DEM data, as visualized in Fig. 1. We implement three UNet variants: vanilla UNet, an improved UNet, and DeepLabv3+ as deep learning baselines and compare them to methods that rely on a single data stream and are used in-practice (Colosio et al., 2020). As the improved UNet achieves 95% accuracy, we also create a daily high-resolution record of surface meltwater fraction over the Helheim Glacier for 2017-2023 that can be used for investigating local ice mass loss processes.

## 2 Data and methods

### 2.1 Study area and period

We focus on a region in Eastern Greenland centered around the Sermilik Fjord, Helheim Glacier (66.4°N, 38.2°W), as visualized in Fig. 2. This marine-terminating glacier has been one of the largest contributors to the GrIS ice discharge (Williams et al., 2021), and may be accelerated by an increase in surface meltwater (Andresen et al., 2012; Stevens et al., 2022). The region is suitable to evaluate downscaling techniques, due to the complex topography, variation between ice- and snow-covered sections, and availability of in-situ station data (Shimada et al., 2016; Antwerpen et al., 2022; Fausto et al., 2021). Within the study area, we focus on the land because mass loss from grounded land ice is a major contributor to sea level rise (Edwards et al., 2021), and sea ice dynamics complicate SAR analysis (Howell et al., 2019). We focus our analysis on 2017-2023, delineated by the start of Sentinel-1 SAR data collection and the end of the utilized RCM reanalysis.



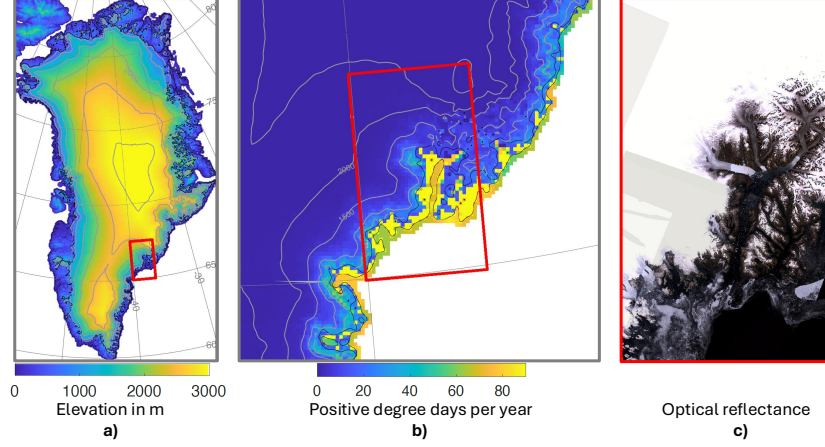


Figure 2: **Study area.** Figure 2a) shows the ice sheet surface elevation over Greenland and our study area (red rectangle) surrounding the Helheim glacier. Figure 2b) shows the number of days per melting season (06/01-08/31) with near-surface air temperature  $>0^{\circ}\text{C}$  averaged over 2017-2023. Figure 2c) shows a satellite imagery mosaic from (I. Howat, 2017a).

## 2.2 Data sources

We download, reproject, and crop all data sources to a 100m Albers equal area projection over our study area, and save them as daily GeoTIFFs (reprojection details in Appendix A). We create a *core* subset of the data that is used for all analyses, and publish a larger *auxiliary* dataset to facilitate follow-up studies that may require a different selection of variables or time periods (Alexander et al., 2024).

### 2.2.1 Synthetic aperture radar (SAR) data

Figure 3 illustrates the estimates of surface meltwater fraction per 100m grid cell that we derive from SAR, during an extreme melt event in 2019. To derive this surface meltwater fraction, we utilized SAR backscatter data from the European Space Agency Sentinel-1A and -1B (S1A and -B) satellites, distributed by NASA’s Earth Observing System Data and Information System (Torres et al., 2017). We used level-1 ground range detected data transmitted and collected in the horizontal polarization, in interferometric wide swath (IW) mode in the C-band (5.405GHz) (Torres et al., 2012). The IW data has a spatial resolution of 5m by 20m and a swath width of 250km. Both satellites have a repeat cycle of 12 days. With multiple satellite tracks intersecting our study area and S1A and S1B being available during 2016-present and 2017-2021, respectively, SAR data partially covers our study area every 1-12 days. The retrieval path boundaries are visible as straight lines between gray and non-grayed area, e.g., in Fig. 3. All S1A and -B data used in our final product were collected between 06:10 and 06:40 local solar time.

Our SAR data workflow is depicted in Fig. A2 and starts with a standard set of processing steps: orbital correction, subsetting, border noise removal, radiometric calibration, speckle filtering, and terrain correction. Then, we reproject the data onto a 10m resolution subset of the 100m Albers equal area grid. We convert backscattering intensity (in dB) to 10m binary melt by applying a threshold of -3dB relative to each year’s winter mean backscatter. This or a similar (-2.8dB) threshold is commonly utilized (Ashcraft & Long, 2006) and consistent with theory and observations (e.g. Johnson et al., 2020; Luckman et al., 2014; Scher et al., 2021; Wismann, 2000; Stiles & Ulaby, 1980). We mosaic all images

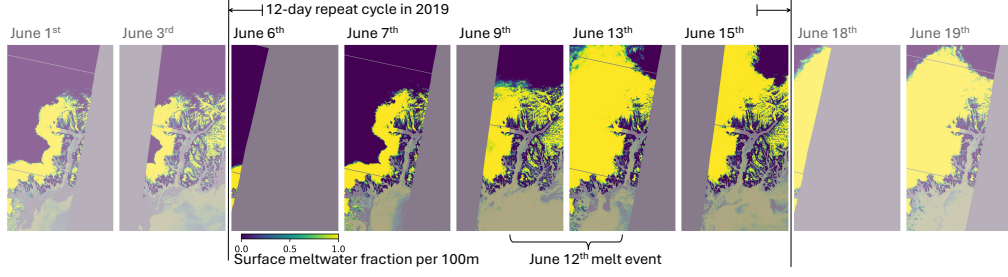


Figure 3: **Surface meltwater targets.** The plots show Sentinel-1 synthetic aperture radar (SAR)-derived surface meltwater fraction per 100m grid cell during an extreme melt event on June 12, 2019 - yellow indicates melt. During this event the melt area across the Greenland ice sheet almost doubled within a single day (Tedesco & Fettweis, 2020) and expanded rapidly across our northwestern study area. We mask out areas that are outside of satellite retrieval paths (gray blocks), over the ocean (southern study area), or impacted by post-processing artifacts (gray lines on June 13).

from the same day into one map and, lastly, aggregate binary 10m melt onto the 100m grid by computing the fraction of 10m cells exhibiting melt within each 100m grid cell.

### 2.2.2 Passive microwave (PMW) data

Satellite-based passive microwave (PMW) measurements are available from 1979 to the present and are commonly used to detect melt on the surface of ice sheets and glaciers (e.g., Abdalati & Steffen, 1995; H. Liu et al., 2005; Tedesco, 2007, 2009; Fettweis et al., 2011; Colosio et al., 2020). We sourced PMW brightness temperature observations from the Special Sensor Microwave Imager/Sounder (SSMIS) at 3.125km resolution using the MEaSUREs product with an effective resolution of 3.125-25km. The SSMIS observations are available every 12 hours - mostly unaffected by local weather - and we select each day’s evening pass ( $\approx 18:30$  local solar time). We detail PMW in Section A2.

### 2.2.3 Regional climate model data (MAR)

We post-process 5km, daily-averaged data from the MARv3.14 regional climate model, which simulates atmospheric dynamics and resolves key processes regarding the ice sheet mass balance (Grailet et al., 2024). The MARv3.14 model incorporates observational data through being forced with six-hourly ERA5 reanalysis data (Hersbach et al., 2020) and having been evaluated against remote sensing and in-situ datasets (e.g., Fettweis et al., 2011, 2020, 2021; Delhasse et al., 2020). We utilize the estimate of liquid water content within the first meter (WA1), which can be used analogous to surface meltwater presence (Kittel et al., 2022; Dethinne et al., 2023). We process and include additional MAR atmospheric variables related to surface meltwater, such as wind speed or shortwave downwelling solar radiation, in the auxiliary dataset. We list these variables in Table A1 and detail MARv3.14 in Section A3.

### 2.2.4 Digital elevation model (DEM), land-ocean mask, and MODIS

Besides dynamic variables, we add a static DEM mosaic at 100m that is generated from panchromatic stereoscopic imagery in 2008-2020 and lidar observations in summer 2019-2020, and is detailed in Section A4. We also use a static 100m land-ocean mask, which is derived from panchromatic and SAR imagery, as detailed in Section A5. We use the land-ocean mask to focus the model evaluation over land only.

We also process daily 500m visible and NIR observations in 4 spectral bands from MODIS Terra, as they could provide key information on surface reflectance changes due to melt and other factors controlling melt, such as the deposition of particulate matter or microbial growth. However, the region experiences frequent cloud cover, limiting the availability of MODIS data. For this reason, we do not use MODIS in our core dataset, but include it in the auxiliary dataset.

### 2.3 Data characteristics

The core dataset contains data from each melting season (Apr 1st - Sep 30th) in 2017-2023, resulting in  $K = 529$  observed days. The non-melting season (Oct 1st - Mar 31st) is retained for selected data streams in the auxiliary dataset. The study area measures  $286.3\text{km} \times 163.3\text{km}$  totaling  $\approx 46,750\text{km}^2$ . After regridding, all input and target images have the same size ( $2863 \times 1633$  pixels) and 100m resolution. The total number of input channels is four in the core dataset (MAR, PMW, DEM, and running mean SAR) with an additional 22 channels in the auxiliary dataset (18x MAR, 4x MODIS). Our core dataset measures  $\sim 20\text{GB}$  at float32, and we intentionally kept it small to medium-sized compared to standard superresolution datasets (see Section A6) to minimize barriers to adoption and reuse. The auxiliary dataset is significantly larger with  $\sim 1.1\text{TB}$  at float64.

Figure 4 shows the target meltwater fraction per day. The targets are represented as single-channel images with values between 0 and 1 that follow a bimodal distribution that is slightly skewed towards pixels with no melting (65:35), as detailed in Fig. A3. The core dataset contains a high percentage of invalid pixels (63%), because each SAR retrieval path does not fully cover the study area (with the % of valid pixels per image in Fig. A4b), and we mask out processing artifacts and ocean-pixels (28% of the study area).

An important characteristic of our dataset is the occurrence of extreme melt events. For example, Fig. A1 presents the data streams that were observed during the extreme melt event on June 12, 2019. During this event, Greenland’s melt area almost doubled from  $\approx 30\%$  to  $55\%$  within a single day (see Fig 2a in Tedesco & Fettweis, 2020). Other extreme melt events are also visible as rapid surges in the observed meltwater fraction in Fig. 4 (e.g., 06/04/2018, 06/12/2019, 09/03/2022). However, the satellite swath patterns also cause significant fluctuations in our observations of meltwater fraction and it becomes unclear whether some extreme melt events are not visible due to data gaps or because melting did not occur over the Helheim area (e.g., 07/31/2019, 07/28/2021, 08/14/2021, 07/18/2022).

### 2.4 Test dataset and evaluation protocol

We create a validation (val) and test split that are stratified across time by randomly sampling two images from each month for each split, from 2018-2023. All leftover images from 2018-2023 are used during training, as well as 2017 during which images only cover the southwestern study area (detailed in Section A6). This results in a (13%, 13%, 74%) split with 70 test, 70 val, and 389 training (train) days. Following common protocol (Goodfellow et al., 2016), we use the train and val set for optimization of free parameters and adapting hyperparameters, respectively. All metrics and plots are reported on the test set unless noted otherwise.

We create the stratified split due to the data imbalance visualized in Fig. A4a. Using this split our evaluation metrics are equally-weighted for any given day in any year, rather than being biased towards heavily-sensed years, such as 2021. The splits also share data from the same years, such that we can evaluate the methods on creating a gap-filled product - as opposed to forecasts. We avoid a cross-validation split, because the associated computational expense of repeatedly retraining models would decrease the accessibility of our proposed benchmark. In summary, we choose this split to evaluate the accuracy of methods to interpolate in time and space, and we discuss future experiments towards devel-

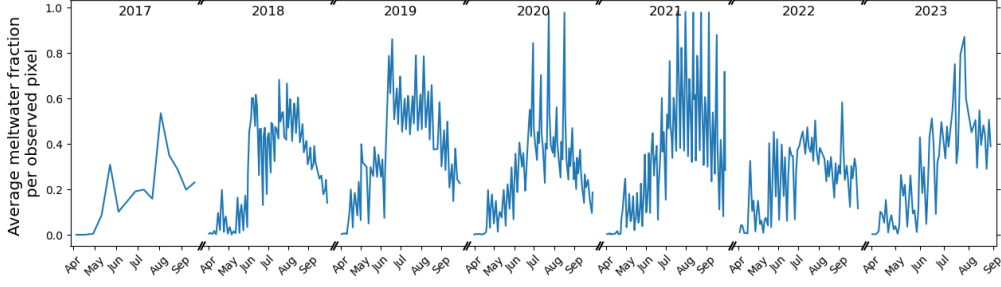


Figure 4: **Target meltwater fraction.** The plot shows the average fraction of surface meltwater per valid pixel for every retrieved SAR observation. A value of 0.7, for example, means that 70% of the land-based study area that was observed on that day, and is not otherwise masked, contains surface meltwater. Strong fluctuations can indicate important melt events (e.g., on June 12, 2019) or noise from alternating satellite swath retrievals that cover different sections of the study area (e.g., 5x peaks from July-Sept, 2021). During 2017, our dataset only covers a subsection of the study area, and during 2022-23 S1B data is unavailable. Tick marks indicate the 1st of each month.

oping methods for forecasting, reconstructing meltwater pre-SAR, and spatial extrapolation in Section 4.2.

## 2.5 Evaluation metrics

Due to the frequent and irregular occurrence of invalid values in our targets, we compute most metrics as averages per valid pixel - as opposed to the more commonly used averages per image. We apply the static land-ocean mask to all model predictions before calculating error metrics or creating plots.

Let  $\mathbf{Y} = \{\mathbf{Y}_k\}_{k=0}^{K-1}$  be the set of target images,  $\mathbf{Y}_k \in [0, 1]^{(I \times J)}$ , with height,  $I$ , width,  $J$ , and timestamp,  $k \in \mathbb{K} = \{0, \dots, K-1\}$ . And, let  $\hat{\mathbf{Y}} = \{\hat{\mathbf{Y}}_k\}_{k=0}^{K-1}$  with  $\hat{\mathbf{Y}}_k \in [0, 1]^{(I \times J)}$  be the corresponding set of predictions. Then, we start the evaluation by visualizing the predictions,  $\hat{\mathbf{Y}}_k$ , and biases,  $\hat{\mathbf{Y}}_k - \mathbf{Y}_k$ , for selected timestamps to gain an intuitive understanding of model skill.

**Spatial MSE and MAE.** We compute the spatial mean square error (MSE) per valid pixel to evaluate pixel-level prediction accuracy. Because MSE is known to encourage blurry results due to the quadratic penalty, we also use the spatial mean absolute error (MAE) which slightly reduces this issue (Subich et al., 2025). The commonly used peak signal-to-noise ratio (PSNR) can be expressed as a function of MSE, and is reported in Table C1. The table also contains the standard deviation of each error, the root mean square error (RMSE), and the coefficient of determination ( $R^2$ ), although we caution against  $R^2$  due to our bimodal distribution. We compute MAE and MSE with:

$$\text{Err}_s(\mathbf{Y}, \hat{\mathbf{Y}}) = \frac{1}{N_{\text{valid}}} \sum_{k \in \mathbb{K}} \left( \sum_{(i,j) \in IJ_{\text{valid},k}} (|y_{k,i,j} - \hat{y}_{k,i,j}|)^p \right) \quad (1)$$

where  $\text{Err}_s$  is the spatial mean  $L^p$  norm which reduces to the MSE for  $p = 2$  and the MAE for  $p = 1$ ;  $|\cdot|$  denotes the absolute value;  $IJ_{\text{valid},k}$  is the set of all (lat, lon) index combinations,  $(i, j)$ , that correspond to valid pixels in the  $k$ -th image;  $N_{\text{valid}} = \sum_{k \in \mathbb{K}} n_{\text{valid},k}$  is the number of valid pixels summed over all images;  $n_{\text{valid},k} = |IJ_{\text{valid},k}| = \sum_{(i,j) \in IJ_{\text{valid},k}} 1$

is the number of valid pixels in the  $k$ -th image;  $y_{k,i,j}$  and  $\hat{y}_{k,i,j}$  are single pixels in range  $[0, 1]$  in the target and predicted images, respectively. In general, we denote a tensor as  $\mathbf{A}$ , a matrix as  $\mathbf{A}$ , and a scalar as  $a$  or  $A$ .

**SSIM.** Since the pixelwise MAE and MSE are less suitable for capturing the stochastic nature of our downscaling problem where multiple plausible high-resolution outputs exist for a single low-resolution input—for example along meltwater boundaries—we also compute the structural similarity index measure (SSIM). The SSIM compares two images by evaluating image statistics on a sliding window basis and ranges between  $[0, 1]$  with best values being 1. To compute the SSIM on our masked images we set all invalid pixels to zero before computing the SSIM. This choice increases scores at the border to invalid pixels, but remains a fair measure for intercomparing models as the location of invalid pixels is independent of the model.

$$\text{SSIM}(\mathbf{Y}, \hat{\mathbf{Y}}) = \frac{1}{N_{\text{valid}}} \sum_{k \in \mathbb{K}} \sum_{(i,j) \in IJ_{\text{valid},k}} \text{ssim}_{\text{im}}(\mathbf{M}_k \odot \mathbf{Y}_k, \mathbf{M}_k \odot \hat{\mathbf{Y}}_k)_{i,j} \quad (2)$$

where  $\mathbf{M}_k \in \mathbb{1}^{(I \times J)}$  is a binary mask with 0 for invalid and 1 for valid pixels;  $\mathbf{Y}_k$  is the ground-truth image tile  $k$ ;  $\hat{\mathbf{Y}}_k$  is the predicted image tile;  $\odot$  denotes an element-wise product. And,  $\text{ssim}_{\text{im}} \in [0, 1]^{(I,J)}$  is a tensor in which each  $(i, j)$ -th pixel contains the value of the corresponding sliding window calculation:

$$\text{ssim}_{\text{im}}(\mathbf{Y}_k, \hat{\mathbf{Y}}_k)_{i,j} = \frac{(2\mu_{\hat{y}}\mu_y + c_1)(2\sigma_{\hat{y}y} + c_2)}{(\mu_{\hat{y}}^2 + \mu_y^2 + c_1)(\sigma_{\hat{y}}^2 + \sigma_y^2 + c_2)} \quad (3)$$

where  $\mu_y$  and  $\mu_{\hat{y}}$  are the mean over a window centered at pixel  $(i, j)$  in tile  $\mathbf{Y}_k$  or  $\hat{\mathbf{Y}}_k$ , respectively (the subscripts are omitted for brevity);  $\sigma_y$  and  $\sigma_{\hat{y}}$  are the standard deviation over all pixels in the same window;  $\sigma_{\hat{y}y}$  is the co-variance between all predicted and ground-truth values in the window; and  $c_1, c_2$  are constants. The sliding window is implemented using a Gaussian kernel with size  $h_w = 72$ , standard deviation  $\sigma_w = 10$ , reflection padding, and constants  $c_1 = 1e-4$  and  $c_2 = 9e-4$ . The sliding window implementation is based on the torchmetrics package (Detlefsen et al., 2022).

**Binary classification metrics.** For interpretability, we also compute classification metrics by categorizing predicted and target surface meltwater fraction into 'no-melt' and 'melt' using a threshold of  $y_{\text{thold}} = 0.1$ . We compute precision ( $\frac{tp}{tp+fp}$ ), recall ( $\frac{tp}{tp+fn}$ ), and accuracy ( $\frac{tp+tn}{tp+tn+fp+fn}$ ), with the abbreviations  $t$ =true,  $f$ =false,  $p$ =positive, and  $n$ =negative. To account for the invalid data masks, we compute the scores as averages across all valid pixels, for example, for accuracy:

$$\text{Acc}(\mathbf{Y}, \hat{\mathbf{Y}}) = \frac{1}{N_{\text{valid}}} \sum_{k \in \mathbb{K}} \sum_{(i,j) \in IJ_{\text{valid},k}} \mathbb{1}[\mathbb{1}(y_{k,i,j} > y_{\text{thold}}) == \mathbb{1}(\hat{y}_{k,i,j} > y_{\text{thold}})] \quad (4)$$

We also compute an F1-score which is the harmonic mean of precision and recall. The equation for each metric is given in Section B1.

**Number of parameters.** We count the number of parameters per model to provide a measure of model complexity. We count the number of weights (i.e., free parameters) and hyperparameters that are adjusted using our training and/or validation dataset and exclude fixed hyperparameters, free parameters fitted using external datasets, and data generating parameters, such as MAR parametrizations or sensor calibrations.

**Monthly statistics.** We evaluate if a model systematically under- or overestimates meltwater across the study area by calculating the monthly-averaged meltwater fraction per valid pixel:

$$\bar{\hat{y}}_m = \frac{1}{|\mathbb{K}_m|} \sum_{k \in \mathbb{K}_m} \frac{1}{n_{\text{valid},k}} \sum_{(i,j) \in IJ_{\text{valid},k}} \hat{y}_{k,i,j} \quad (5)$$

whereas  $|\mathbb{K}_m|$  is the number of images in month,  $m$ , and all years and  $\mathbb{K}_m$  indexes those image.

## 2.6 Downscaling methods

We implement several traditional methods that are used in practice and compare them with UNet-based deep learning architectures.

### 2.6.1 Traditional methods

**Running mean SAR.** The running mean SAR model assumes that the meltwater fraction at any unobserved target date is approximately the running monthly mean of all observations surrounding the target date, as detailed in Section B2. This model uses only imagery from the training set as inputs to avoid data leakage during validation or test. The predictions of this model are also used as inputs to the deep learning-based models in most of our experiments.

**Interpolate MAR.** The interpolate MAR model assumes that the meltwater fraction equals the MAR-modeled average liquid water content within the top meter of snow after applying a Gaussian blur and adjusting the intensity, as detailed in Section B3. We interpret this model as the surface meltwater fraction predicted by the MAR model.

**Threshold PMW.** The threshold PMW model is binary and detects meltwater if the brightness temperature at a given location exceeds a threshold that is based on the winter mean brightness temperature and a fixed output of a microwave emission model of layered snowpack, as detailed in Section B4. This method is commonly used in large-scale studies across Greenland (Colosio et al., 2020).

**Threshold DEM.** The threshold DEM model assumes that all locations within a monthly varying elevation band contain meltwater, as detailed in Section B5. This follows the intuition that higher altitudes will exhibit colder temperatures and lower altitudes are more likely to feature exposed rock, registering less melt, while the intermediate area may be melting.

### 2.6.2 Deep learning-based downscaling methods

**UNet.** We implemented a UNet-based model (Ronneberger et al., 2015), because it is a commonly used model architecture to approach image-to-image translation problems using an  $L_p$ -norm (Sha et al., 2020), adversarial (Isola et al., 2017), or diffusion-based (Saharia et al., 2023) loss function, and continues to achieve competitive results on medium-sized datasets (Isensee et al., 2021). The UNet architecture is designed to learn small and large-scale spatial correlations by using an encoder-decoder architecture with skip connections, as visualized for a vanilla UNet in Fig. B1. Further, using convolutional layers introduces a theoretically beneficial spatial locality bias (Cachay et al., 2021). The UNet learns the mapping,  $f_\theta : \mathbf{X}_k \rightarrow \mathbf{Y}_k$ , with the inputs,  $\mathbf{X}_k \in \mathbb{R}^{n_c \times w \times h}$ , that have  $n_c = 4$  input channels (MAR WA1, PMW, DEM, Time-interpolate SAR) and outputs,  $\mathbf{Y}_k \in \mathbb{R}^{w \times h}$ , that is the surface meltwater fraction, as displayed in Fig. 1. Instead of using the full study area in the in- and outputs, we train the UNet model on fixed-size tiles with size  $(w \times h)$ . We train the model to minimize a masked  $L_1$ -loss that is given by Eq. (1) with  $p = 1$  and  $K$  equal to the batch size.

To train the UNet, we implemented a dataloader that randomly generates locations from which to extract the tiles from within the study area. These tile locations are resam-



pled for every image and epoch, whereas one epoch contains one tile of every image in the dataset. In comparison with the commonly used approach of precomputing and storing tiles on disk (Stengel et al., 2020), this dynamic tiling approach reduces redundant storage and, more importantly, can be seen as a form of data augmentation that encourages translation equivariance. Memory consumption does not become an issue due to GeoTIFFs supporting windowed reading. During validation and test, we create a full-size image mosaic by convolve the learned model across the study area with a stride,  $s$ , and merging predictions by computing the average value at every overlapping pixel. We erode the outer  $e$  pixels before mosaicing, because the accuracy of CNN-based predictions is known to deteriorate towards image borders. For tuning hyperparameters, we compute all evaluation metrics on the mosaic and use SSIM to select the best model configuration.

**Model optimization.** We distinguish our experiments to optimize the UNet as: ‘vanilla UNet’, ‘DeepLabv3+’, and ‘UNet SMP’. The vanilla UNet follows (Ronneberger et al., 2015), for the most part and is detailed in Section B6. Using the vanilla UNet, we ran early experiments on the choice of loss function,  $L_1$  vs  $L_2$ , tile size,  $[64, 128, 256, 512]$ , and preprocessing steps, and observed the best SSIM scores with an  $L_1$ -loss, tile size  $h = w = 512$ , and a Gaussian blur that smooths MAR and PMW inputs. The vanilla UNet is comparatively shallow, trained from scratch, and has a receptive field that limits the maximum learnable spatial correlations to 188px, as detailed in Section B6. Thus, we follow (L.-C. Chen et al., 2018) using the segmentation models pytorch (SMP) library to implement DeepLabv3+ and UNet SMP, which both use a deeper encoder with pretrained weights. DeepLabv3+ uses a special module in the bottleneck that extracts multi-scale features using dilated convolutions (called atrous spatial pyramid pooling) but limits the reference implementation to  $h = w = 304$ px. Thus, we still optimize the commonly used hyperparameters in DeepLabv3+, but focus further experiments on UNet SMP. The final model, UNet SMP from now on referred to as ‘UNet’, uses  $h = w = 512$ ,  $s = 480$ ,  $e = 16$ , ImageNet-pretrained weights, and an xception71 encoder, with the full set of parameters detailed in Section B7.

### 3 Results

In Section 3.1, we demonstrate that the UNet and time-interpolate SAR models resolve surface meltwater at higher spatial resolution and evaluation scores than the threshold PMW and interpolate MAR models. In Section 3.2, we show that the PMW- and MAR-based models over- or underestimate meltwater during selected months with respect to the SAR-derived targets, whereas the UNet and time-interpolate SAR model can capture the seasonal meltwater variation more accurately. In Section 3.3, we analyse the generated product for every day in the melting seasons of 2017-2023. In Appendix C, we also report on the difference between the deep learning-based models.

#### 3.1 High-resolution features in model predictions

Figure 5a and Fig. 5b show a map of each model’s surface meltwater prediction and bias for a selected date in June, 2018. Every model’s predictions have the same high-level features: The models generate predictions over the date’s unobserved pixels (gray area), correctly predict a region of no-meltwater in high elevations (Northern deep blue area), and predict significant melting at medium-to-low elevations (contiguous yellow area) toward the ocean. Predicting high-resolution details along meltwater boundaries and the mountainous coast seems more challenging: The interpolate MAR and threshold PMW predictions are too coarse and limited by their native resolution of 3-5km. The time-interpolate SAR prediction resolves high-resolution features at 100m/px, but contains postprocessing artifacts (blue lines or sharp green-to-blue transitions). The UNet model resolves high-resolution features with similar biases as time-interpolate SAR, e.g., along the Northern meltwater boundary, but is able to partially correct for some postprocessing artifacts.

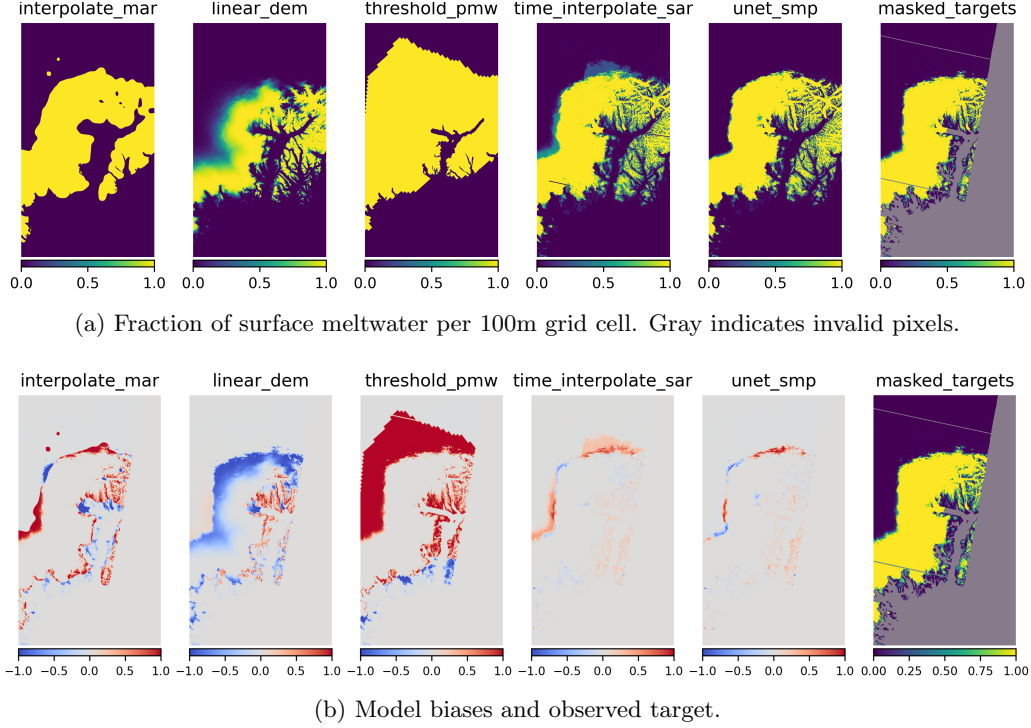


Figure 5: **High-resolution predictions and biases.** Prediction (top) and bias (bottom) of each model (left 5 columns) and observed meltwater target (rightmost column) for a date in the test dataset (June 24, 2018). Model biases are calculated as prediction minus target, such that red and blue indicate over- and underestimated values, respectively. The input data streams for this date are displayed in Fig. 1, and the date was selected to highlight each model’s characteristics.

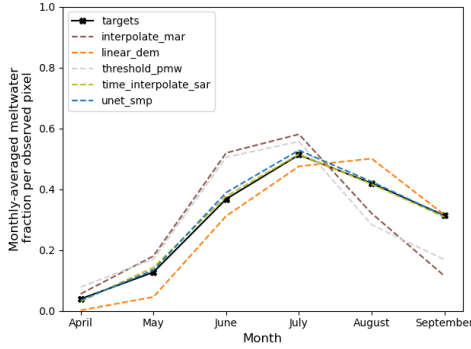
Table 1 shows that the deep learning models (vanilla UNet, UNet, and DeepLabv3+) and time-interpolate SAR achieve the best evaluation scores across our study area and observations in the test dataset. Most of the scores are computed on a per-pixel basis, meaning that high scores are likely to be associated with a model’s capability for predicting high-resolution features. Notably, the UNet achieves an accuracy of 95% which significantly improves on the operational threshold PMW model (72%) and a naïve model that would always predict no-melt (65%). The UNet outperforms time-interpolate SAR in terms of error metrics by achieving a  $\sim 40\%$  lower MAE and predicting fewer false positives (as indicated by the improved precision at comparable recall in Table C1). However, the UNet model has 49.6M free parameters which is significantly more than time-interpolate SAR, and can be an important evaluation criterion (see Section 4.2).

### 3.2 Temporal biases in meltwater predictions

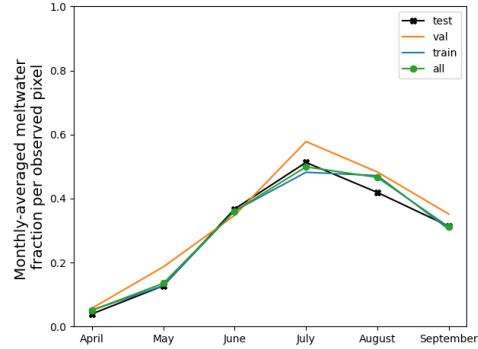
To uncover temporal biases, we plot the predicted and observed surface meltwater fraction per month in Fig. 6a. Notably, interpolate MAR (brown) and threshold PMW (gray) both overpredict meltwater in early summer (June) and underpredict it in late summer (Sept) with respect to the SAR targets. The UNet (blue) and time-interpolate SAR (green) more accurately match the SAR observations (solid black) in terms of the average monthly surface meltwater fraction across the study period. Other differences (e.g., in June) are not

Table 1: **Results table.** Evaluation scores on test dataset by model, with #p denoting the number of parameters. The last row reports the average difference between the models’ val and test scores to suggest a necessary score difference for determining that a model is better beyond data noise. Best scores within the test-val score difference are **bold**, next-best *italic*, reported to three significant digits, with standard deviations in Table C1. ‘UNet SMP’ is abbreviated as ‘UNet’.

Model	#p. ↓	MAE <sub>s</sub> ↓	MSE <sub>s</sub> ↓	Acc. ↑	F1 ↑	SSIM <sub>σ=10</sub> ↑
Time-interpolate SAR	<b>1</b>	0.0778	0.0389	0.899	0.812	<i>0.711</i>
Interpolate MAR	<i>4</i>	0.167	0.149	0.826	0.664	0.493
Threshold PMW	<b>0</b>	0.272	0.254	0.724	0.557	0.423
Threshold DEM	12	0.187	0.137	0.813	0.699	0.462
DeepLabv3+	42.9M	<i>0.0572</i>	<i>0.0331</i>	<i>0.935</i>	<i>0.830</i>	0.711
UNet	49.6M	<b>0.0474</b>	<b>0.0250</b>	<b>0.946</b>	<b>0.848</b>	<b>0.762</b>
vanilla UNet	31.0M	<i>0.0594</i>	<i>0.0356</i>	<i>0.934</i>	<b>0.840</b>	<i>0.744</i>
test-val score difference	n/a	0.00475	0.00474	0.00480	0.0120	0.00574



(a) UNet and traditional methods



(b) Monthly distribution across data splits

Figure 6: **Average meltwater fraction over a melting season.** Fig. a) shows the target (black) and predicted monthly-averaged surface meltwater fraction per valid pixel, averaged across 2017-2023. Fig. b) shows the same quantity but averaged across the train, val, test, and entire dataset to illustrate the magnitude of variation between data splits.

interpreted, because they are smaller than the variation between data splits in Fig. 6b, and would not necessarily persist on resampled data splits.

### 3.3 Gap-filled surface meltwater product

After training, we query each model to predict a map of surface meltwater for every day in the study period. Figure 7 shows the area that lies within the study area and is predicted to be covered by meltwater. In this plot there are no targets because the SAR retrieval paths only intersect with subsections of the study area. But, for completeness we plot the predicted meltwater fraction per observed pixel against the comparatively noisy test set targets Fig. C1.

Figure 7a shows that extreme melt events are visible in the UNet-predicted gap-filled meltwater product as sharp increases, e.g., during the event on June 12, 2019. Moreover, some extreme melt events, e.g., Aug. 14, 2021 (Moon et al., 2021) are challenging to dis-

tinguish from noise in the sporadic SAR observations (Fig. 4) and the PMW-based product (Fig. 7b), whereas their impact on meltwater surrounding the Helheim Glacier is visible in the UNet and MAR-based products in Fig. 7b.

The time-interpolate SAR model predicts less meltwater than the UNet on extreme melt days, e.g., on June 12, 2019, which is likely due to the method’s moving window average. There are also step function artifacts in the time-interpolate SAR predictions, e.g., in mid-June 2019, but they could likely be removed by using a larger window average. In 2017, time-interpolate SAR predicts significantly less meltwater coverage than the other methods, which is due to the SAR targets over the Eastern part of our study area being masked throughout the whole year.

A video demonstrates the UNet-created product of daily 100m maps from 2018-2023, and is accessible in the supplementary material and at this link. The video illustrates the seasonal changes in surface meltwater distribution and effects of the coastlines and topography. The visible high-resolution dynamics include the redistribution of meltwater towards the Helheim glacier’s border in the late season. The video also demonstrates some artifacts from the UNet’s prediction stride and SAR processing artifacts.

### 3.4 Deep learning hyperparameter insights

Tuning the hyperparameters of the deep learning models required a sizable amount of computations, and increased the scores, e.g., of the UNet from an off-the-shelf performance of 0.715 to 0.762 SSIM. Here, we report our insights on the optimal hyperparameters in anecdotal fashion because a full documentation is beyond the scope of this paper: Notably, increasing the tile size, in particular from 64 to 256px, improved the vanilla UNet performance, which indicates a capability of the deep learning models to correct large-scale biases. Further, using ImageNet-pretrained instead of randomly initialized weights slightly increased scores (0.01 – 0.02 SSIM) across models (UNet, DeepLabv3+) and backbone choices (xception, resnet), which may be surprising due to the substantial domain shift between natural and geospatial imagery in ImageNet and MeltwaterBench (Rolf et al., 2024). Choosing deeper encoders (xception-41, -65, -71) also improved SSIM evaluation scores. One training run of the UNet takes 16.5 hours on 1x V100 GPU; with 1085 epochs, 500 tiles/epoch, 512px tiles, and 100m/px. Inference time is significantly faster and, assuming a linear scaling of compute by processed area, running inference across all of Greenland ( $\sim 2\text{M km}^2$ ) would take on the order of tens of minutes to hours. Additional hyperparameter insights are detailed in Section C3.

## 4 Discussion

### 4.1 Implications of seasonal bias for process-based models

Our results in Fig. 6a have shown that current MAR- and PMW-based methods have a systematic seasonal bias in estimating the Helheim glacier’s distribution of surface meltwater, in comparison to SAR-derived targets. These biases could stem from differences in the instruments: SAR might be more sensitive than PMW to deep liquid water accumulation in the late season, whereas PMW may be more sensitive to early season shallow meltwater. Further, MAR is consistent with PMW similar to past studies that have also analysed MAR outputs over the top 1 m of snow (Dethinne et al., 2023).

Additionally, the seasonal biases may result from processes that are not sufficiently captured in MAR: The underestimation of meltwater in late summer by MAR, in particular, might be due to light-absorbing impurities, which are not accounted for in the model, leading to an overestimation of albedo (Antwerpen et al., 2022). Another reason might be the so-called “mixed pixel effect”: for example, if a 3-25km PMW pixel contains a mixture of rock and snow, and the rock heats up faster during early summer, it can skew the pixel’s average

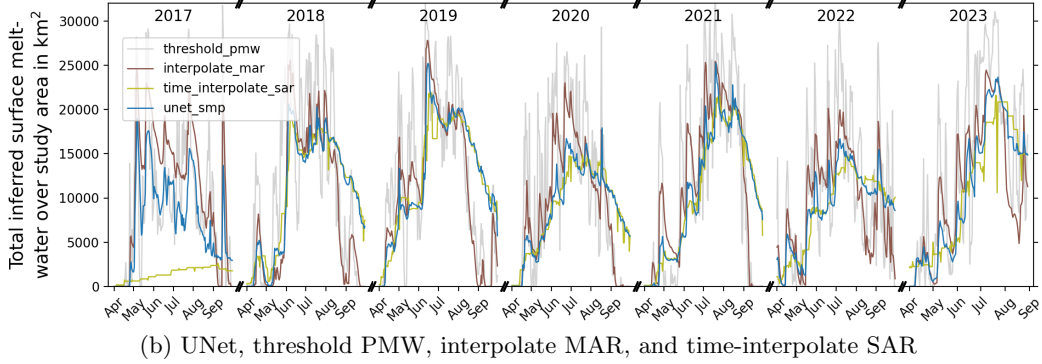
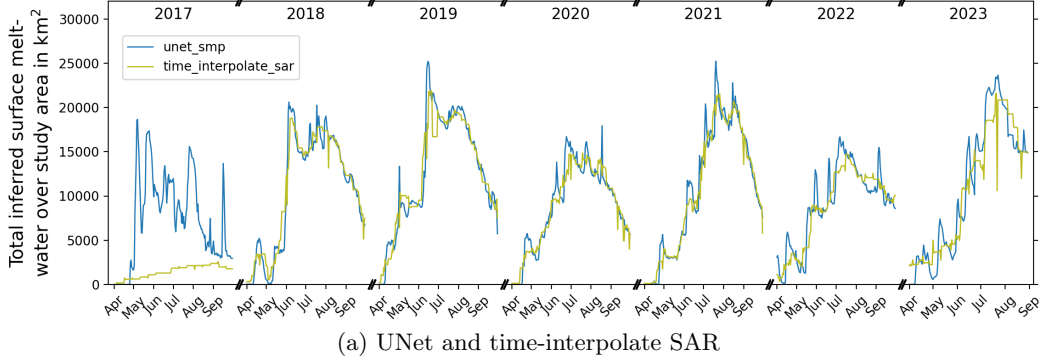


**Figure 7: Predictions of surface meltwater for every day in the 2017-2023 study period.** Predicted total area of surface meltwater within the study area for the UNet (blue), time-interpolate SAR (yellow), threshold PMW (gray), and interpolate MAR (brown) model. Vanilla UNet and DeepLabv3+ are reported in Fig. C2. Sharp increases in total meltwater, such as on June 12, 2019, indicate extreme melt events. The target observations are not plotted due to their spatiotemporal gaps. Tick marks indicate the 1st of each month.

over the melt-threshold despite the snow not having melted, yet. This would imply that km-scale data from PMW or MAR can exhibit biases over a smaller spatial domain that could also affect other sites in Greenland. Our analysis in Fig. 6a has shown that the UNet is capable of accounting for these seasonal biases and correcting them - creating a product that more closely resembles SAR.

Another reason for the seasonal bias may be our data selection: Our benchmark contains SAR data from the morning hours, PMW data from the evening, and daily averages from MAR. Some of the over- (under-) estimation of PMW and MAR during the peak (late) melting season may be attributable to melting (snowfall) that occurs throughout the day. We could have chosen the PMW morning pass to allow for a closer comparison between the SAR and PMW sensors. But, PMW and SAR observations are not guaranteed to be temporally-aligned in other areas, and our experiments on the evening pass demonstrate that the UNet can account for the systematic bias introduced by this commonly-occurring temporal mismatch.

#### 4.2 Limitations of the benchmark and daily gap-filled product

The data-driven downscaling models described in this paper are fundamentally constrained by the accuracy of the “ground-truth” surface meltwater targets, which we derive from SAR backscatter intensity using a threshold-based approach. SAR is generally considered one of the most accurate methodologies for inferring surface meltwater presence due to its high resolution (10m), sensitivity to liquid water, and indifference to cloud presence. But, SAR-derived meltwater estimates can contain inaccuracies due to local variations in the optimal threshold, radiative scattering from surrounding mountains, or the ambiguity between surface and subsurface melting. While improving the calibration of SAR-derived meltwater estimates remains an important research direction, our work addresses the complementary challenge of developing spatiotemporal interpolation techniques.

There are many machine learning techniques which may further improve the interpolation: For example, our UNet is not capable of accurately predicting events that occur on small temporal *and* small spatial scales, such as the rapid drainage of small (<250m) lakes (Miles et al., 2017), as they are unresolved in the daily input data streams and the model is deterministic. Generative methods, such as diffusion models, have the potential to overcome this issue by learning distributions between a low-resolution input and multiple possible high-resolution targets (Li et al., 2022). Furthermore, the UNet inputs exclude possibly relevant information, such as atmospheric patterns or the timestamps of SAR observations, which could be overcome by more complex inputs and spatiotemporal model architectures. As evaluating the full suite of possibilities and novel ML methods goes beyond the scope of this study, we encourage MeltwaterBench to be used for intercomparing advances in meltwater downscaling algorithms.

The UNet has almost 50M parameters, which stands in contrast with the single parameter of the running mean SAR baseline. The lower parameter count greatly simplifies the interpretability. And, given the considerable accuracy of the SAR-based baseline it may be sufficient to use a purely SAR-based product for some applications. But, we remind that operational SAR data is not available at daily temporal scales, meaning that the purely SAR-based interpolation smooths out extreme melt events, as in Fig. 7.

Our proposed benchmark evaluates a model’s ability to fill in spatiotemporal gaps in meltwater observations, but does not evaluate a model’s capability to forecast, hindcast, or generalize to other locations. In particular, meltwater within our study area primarily accumulates in the snowpack which results in large areas that are detected as meltwater. In contrast, on the southwestern GrIS meltwater accumulates in ponds and streams meaning a model that is trained on the southeastern GrIS would not necessarily generalize to these new conditions. Also, a generalization to Antarctica, such as the Larsen C ice shelves, would need to include the importance of winds.

#### 4.3 Extensions of deep learning-based downscaling of meltwater

Evaluating the deep learning method across climatic zones would also be necessary to extend our work from surface meltwater estimates to ice sheet mass loss. Estimating mass loss would further require scaling the computations to all of Greenland and establishing a link to annual runoff. Promisingly, the computational cost seems feasible based on Section 3.4 and a link to runoff may be achievable through statistical fits to point observations or RCM estimates of runoff volume (de Roda Husman et al., 2024b).

We suggest two cases that may benefit from the high spatiotemporal resolution of our methodology: First, quantifying the drivers of regional rapid melt events. In particular, retraining the UNet using winds and temperature from multiple days preceding melt events could facilitate sensitivity analyses between coastal melting and large-scale synoptic weather patterns, such as blocking events and atmospheric rivers. Second, the daily 100m information on meltwater across the Helheim glacier may assist with analyzing how local meltwater



distribution impacts glacier flow and basal friction. Studies often rely on point measurements of meltwater (Stevens et al., 2022) and the gap-filled product may help contextualize those to melting in surrounding areas.

## 5 Conclusion

We demonstrated that deep learning methods can improve on conventional algorithms for downscaling surface meltwater. In particular, deep learning can enhance regional climate model estimates of surface meltwater fraction by incorporating remote sensing datasets from SAR and PMW. The created daily 100m resolution maps of Helheim glacier’s surface meltwater may aid in revealing insights about ice mass loss processes. More broadly, deep learning shows promise towards improving mass balance assessments across the Greenland ice sheet and we hope MeltwaterBench can encourage further advances in downscaling algorithms.

## 6 Reproducibility and data availability statement

The code is published at [github.com/blutjens/hrmelt](https://github.com/blutjens/hrmelt) and associated with a CC BY-NC 4.0 license. The core dataset is published at [huggingface.co/datasets/blutjens/hrmelt](https://huggingface.co/datasets/blutjens/hrmelt), and the auxiliary dataset is distributed through the U.S. Antarctic Program Data Center (USAP-DC) at [usap-dc.org/view/dataset/601841](https://usap-dc.org/view/dataset/601841). Users of the core or auxiliary dataset are asked to reference this paper, as well as the data reference (Alexander et al., 2024). The core and auxiliary dataset are published with a CC BY-4.0 license. The created daily 100m product is available as geotiffs on [huggingface](https://huggingface.co/datasets/blutjens/hrmelt) (2017-23) and as video (2018-23) at [youtu.be/OaonUT6dIbg](https://youtu.be/OaonUT6dIbg) with CC BY-4.0. Data from the Programme for Monitoring of the Greenland Ice Sheet (PROMICE) are provided by the Geological Survey of Denmark and Greenland (GEUS) at [promice.org/weather-stations](https://promice.org/weather-stations) under a CC-BY-4.0 license.

## Author Contributions

B.L. is the lead author and contributed to all CRediT author roles. P.A. processed the datasets and together with R.A. contributed to data curation, formal analysis, investigation, methodology, software, validation, and writing - original draft and writing - review and editing. T.W. contributed to software in the form of conducting the DeepLabv3+ experiment. G.C. contributed to conceptualization, formal analysis, funding acquisition, and writing - review and editing. M.T. contributed to conceptualization, funding acquisition, formal analysis, validation, and writing - review and editing.

## Acknowledgments

This material is based upon work supported by the National Science Foundation Early-Concept Grants for Exploratory Research (NSF EAGER) under Grant No. (2136938). We appreciate USAP-DC, PROMICE, GEUS, ESA, Copernicus, NSIDC, among others for their open data policies. We are very grateful to Xavier Fettweis for providing the MAR data, and to Justin Kay and Matthew Kearney for conducting initial experiments on diffusion-based models. Thank you to Dava Newman for the help in funding acquisition and encouraging this work.

## References

- Abdalati, W., & Steffen, K. (1995). Passive microwave-derived snow melt regions on the Greenland ice sheet. *Geophysical Research Letters*, 22(7), 787–790. Retrieved from <https://doi.org/10.1029/95GL00433>
- Abraham, S. (2025). Physics-informed graph diffusion for climate downscaling. In *Women in machine learning workshop @ neurips 2025*. Retrieved from <https://openreview.net/>

- forum?id=PsMONSydIp
- Agustsson, E., & Timofte, R. (2017). NTIRE 2017 Challenge on Single Image Super-Resolution: Dataset and Study. In *Proceedings of the IEEE conference on computer vision and pattern recognition (cvpr) workshops*. Retrieved from <https://doi.org/10.1109/CVPRW.2017.150>
- Alexander, P. M., Antwerpen, R., Cervone, G., Fettweis, X., Lütjens, B., & Tedesco, M. (2024). *Surface melt-related multi-source remote-sensing and climate model data over Helheim Glacier, Greenland*. U.S. Antarctic Program (USAP) Data Center. Retrieved from <https://doi.org/10.15784/601841>
- Andresen, C. S., Straneo, F., Ribergaard, M. H., Bjørk, A. A., Andersen, T. J., Kuijpers, A., ... others (2012). Rapid response of Helheim Glacier in Greenland to climate variability over the past century. *Nature Geoscience*, 5(1), 37–41. Retrieved from <https://doi.org/10.1038/ngeo1349>
- Antwerpen, R. M., Tedesco, M., Fettweis, X., Alexander, P., & van de Berg, W. J. (2022). Assessing bare-ice albedo simulated by MAR over the Greenland ice sheet (2000–2021) and implications for meltwater production estimates. *The Cryosphere*, 16(10), 4185–4199. Retrieved from <https://doi.org/10.5194/tc-16-4185-2022>
- Aschwanden, A., Fahnestock, M. A., Truffer, M., Brinkerhoff, D. J., Hock, R., Khroulev, C., ... Khan, S. A. (2019). Contribution of the greenland ice sheet to sea level over the next millennium. *Sci. Adv.*, 5(6). Retrieved from <https://doi.org/10.1126/sciadv.aav9396>
- Ashcraft, I. S., & Long, D. G. (2006). Comparison of methods for melt detection over Greenland using active and passive microwave measurements. *International Journal of Remote Sensing*, 27(12), 2469–2488. Retrieved from <https://doi.org/10.1080/01431160500534465>
- Bailey, H., & Hubbard, A. (2025). Snow mass recharge of the greenland ice sheet fueled by intense atmospheric river. *Geophysical Research Letters*, 52(5). Retrieved from <https://doi.org/10.1029/2024GL110121>
- Briner, J. P., Cuzzzone, J. K., Badgley, J. A., Young, N. E., Steig, E. J., Morlighem, M., ... Nowicki, S. (2020). Rate of mass loss from the Greenland Ice Sheet will exceed Holocene values this century. *Nature*, 586(7827), 70–74. Retrieved from <https://doi.org/10.1038/s41586-020-2742-6>
- Brodzik, M. J., Long, D. G., Hardman, M. A., Paget, A., & Armstrong, R. (2016). MEASURES Calibrated Enhanced-Resolution Passive Microwave Daily EASE-Grid 2.0 Brightness Temperature ESDR, Version 1. *NASA National Snow and Ice Data Center Distributed Active Archive Center*. Retrieved from <https://doi.org/10.5067/MEASURES/CRYOSPHERE/NSIDC-0630.001>
- Cachay, S. R., Erickson, E., Buckner, A. F. C., Pokropek, E., Potosnak, W., Bire, S., ... Lütjens, B. (2021). *The world as a graph: Improving el niño forecasts with graph neural networks*. arXiv. Retrieved from <https://arxiv.org/abs/2104.05089>
- Chen, L.-C., Zhu, Y., Papandreou, G., Schroff, F., & Adam, H. (2018). Encoder-decoder with atrous separable convolution for semantic image segmentation. In *Proceedings of the European conference on computer vision (ECCV)*. Retrieved from [https://doi.org/10.1007/978-3-030-01234-2\\_49](https://doi.org/10.1007/978-3-030-01234-2_49)
- Chen, X., Feng, K., Liu, N., Ni, B., Lu, Y., Tong, Z., & Liu, Z. (2022). RainNet: A Large-Scale Imagery Dataset and Benchmark for Spatial Precipitation Downscaling. In S. Koyejo, S. Mohamed, A. Agarwal, D. Belgrave, K. Cho, & A. Oh (Eds.), *Advances in neural information processing systems* (Vol. 35, pp. 9797–9812). Curran Associates, Inc. Retrieved from <https://dl.acm.org/doi/10.5555/3600270.3600982>
- Colosio, P., Tedesco, M., Fettweis, X., & Ranzani, R. (2020). Surface melting over the Greenland ice sheet from enhanced resolution passive microwave brightness temperatures (1979–2019). *The Cryosphere Discussions*, 2020, 1–41. Retrieved from <https://doi.org/10.5194/tc-15-2623-2021>
- Delhasse, A., Beckmann, J., Kittel, C., & Fettweis, X. (2024). Coupling MAR (Modèle

- Atmosphérique Régional) with PISM (Parallel Ice Sheet Model) mitigates the positive melt–elevation feedback. *The Cryosphere*, 18(2), 633–651. Retrieved from <https://doi.org/10.5194/tc-18-633-2024>
- Delhasse, A., Kittel, C., Amory, C., Hofer, S., Van As, D., S. Fausto, R., & Fettweis, X. (2020). Brief communication: Evaluation of the near-surface climate in ERA5 over the Greenland Ice Sheet. *The Cryosphere*, 14(3), 957–965. Retrieved from <https://doi.org/10.5194/tc-14-957-2020>
- de Roda Husman, S., Hu, Z., van Tiggelen, M., Dell, R., Bolibar, J., Lhermitte, S., ... Munneke, P. K. (2024b). Physically-informed super-resolution downscaling of antarctic surface melt. *Journal of Advances in Modeling Earth Systems*, 16(7). Retrieved from <https://doi.org/10.1029/2023MS004212>
- de Roda Husman, S., Lhermitte, S., Bolibar, J., Izeboud, M., Hu, Z., Shukla, S., ... Wouters, B. (2024a). A high-resolution record of surface melt on antarctic ice shelves using multi-source remote sensing data and deep learning. *Remote Sensing of Environment*, 301, 113950. Retrieved from <https://doi.org/10.1016/j.rse.2023.113950>
- Dethinne, T., Glaude, Q., Picard, G., Kittel, C., Alexander, P., Orban, A., & Fettweis, X. (2023). Sensitivity of the MAR regional climate model snowpack to the parameterization of the assimilation of satellite-derived wet-snow masks on the Antarctic Peninsula. *The Cryosphere*, 17(10), 4267–4288. Retrieved from <https://doi.org/10.5194/tc-17-4267-2023>
- Detlefsen, N. S., Borovec, J., Schock, J., Harsh, A., Koker, T., Liello, L. D., ... Falcon, W. (2022). *TorchMetrics - Measuring Reproducibility in PyTorch*. Retrieved from <https://doi.org/10.21105/joss.04101>
- Edwards, T. L., Nowicki, S., Marzeion, B., Hock, R., Goelzer, H., Seroussi, H., ... others (2021). Projected land ice contributions to twenty-first-century sea level rise. *Nature*, 593(7857), 74–82. Retrieved from <https://doi.org/10.1038/s41586-021-03302-y>
- Fausto, R. S., van As, D., Mankoff, K. D., Vandecrux, B., Citterio, M., Ahlstrøm, A. P., ... Box, J. E. (2021). Programme for Monitoring of the Greenland Ice Sheet (PROMICE) automatic weather station data. *Earth System Science Data*, 13(8), 3819–3845. Retrieved from <https://doi.org/10.5194/essd-13-3819-2021>
- Fettweis, X., Box, J. E., Agosta, C., Amory, C., Kittel, C., Lang, C., ... Gallée, H. (2017). Reconstructions of the 1900–2015 Greenland ice sheet surface mass balance using the regional climate MAR model. *The Cryosphere*, 11(2), 1015–1033. Retrieved from <https://doi.org/10.5194/tc-11-1015-2017>
- Fettweis, X., Hofer, S., Krebs-Kanzow, U., Amory, C., Aoki, T., Berends, C. J., ... others (2020). GrSMBMIP: intercomparison of the modelled 1980–2012 surface mass balance over the Greenland Ice Sheet. *The Cryosphere*, 14(11), 3935–3958. Retrieved from <https://doi.org/10.5194/tc-14-3935-2020>
- Fettweis, X., Hofer, S., Séférian, R., Amory, C., Delhasse, A., Doutreloup, S., ... others (2021). Brief communication: Reduction in the future Greenland ice sheet surface melt with the help of solar geoengineering. *The Cryosphere*, 15(6), 3013–3019. Retrieved from <https://doi.org/10.5194/tc-15-3013-2021>
- Fettweis, X., Tedesco, M., van den Broeke, M., & Ettema, J. (2011). Melting trends over the Greenland ice sheet (1958–2009) from spaceborne microwave data and regional climate models. *The Cryosphere*, 5(2), 359–375. Retrieved from <https://doi.org/10.5194/tc-5-359-2011>
- Filipponi, F. (2019). Sentinel-1 GRD preprocessing workflow. *Proceedings*, 18(1). Retrieved from <https://doi.org/10.3390/ECRS-3-06201>
- Fox-Kemper, B., Hewitt, H., Xiao, C., Adalgeirsdottir, G., Drijfhout, S., Edwards, T., ... Yu, Y. (2021). Ocean, Cryosphere and Sea Level Change [Book Section]. In V. Masson-Delmotte et al. (Eds.), *Climate change 2021: The physical science basis. contribution of working group I to the sixth assessment report of the intergovernmental panel on climate change* (p. 1211–1361). Cambridge, UK and New York, NY, USA: Cambridge University Press. Retrieved from <https://doi.org/10.1017/9781009157896.011>

- Goodfellow, I., Bengio, Y., & Courville, A. (2016). *Deep Learning*. MIT Press. Retrieved from <http://www.deeplearningbook.org>
- Grailet, J.-F., Hogan, R. J., Ghilain, N., Fettweis, X., & Grégoire, M. (2024). Inclusion of the ECMWF ecRad radiation scheme (v1.5.0) in the MAR model (v3.14), regional evaluation for Belgium and assessment of surface shortwave spectral fluxes at Uccle observatory. *EGUsphere*, 2024, 1–33. Retrieved from <https://doi.org/10.5194/egusphere-2024-1858>
- Häkkinen, S., Hall, D. K., Shuman, C. A., Worthen, D. L., & DiGirolamo, N. E. (2014). Greenland ice sheet melt from MODIS and associated atmospheric variability. *Geophysical Research Letters*, 41(5), 1600–1607. Retrieved from <https://doi.org/10.1002/2013GL059185>
- Harder, P., Hernandez-Garcia, A., Ramesh, V., Yang, Q., Sattegeri, P., Szwarcman, D., ... Rolnick, D. (2023). Hard-constrained deep learning for climate downscaling. *Journal of Machine Learning Research*, 24(365), 1–40. Retrieved from <http://jmlr.org/papers/v24/23-0158.html>
- He, K., Zhang, X., Ren, S., & Sun, J. (2015). Delving Deep into Rectifiers: Surpassing Human-Level Performance on ImageNet Classification. In *2015 IEEE International Conference on Computer Vision (ICCV)* (p. 1026-1034). Retrieved from <https://doi.org/10.1109/ICCV.2015.123>
- Hermann, M., Papritz, L., & Wernli, H. (2020). A Lagrangian analysis of the dynamical and thermodynamic drivers of large-scale Greenland melt events during 1979–2017. *Weather and Climate Dynamics*, 1(2), 497–518. Retrieved from <https://doi.org/10.5194/wcd-1-497-2020>
- Hersbach, H., Bell, B., Berrisford, P., Hirahara, S., Horányi, A., Muñoz-Sabater, J., ... others (2020). The ERA5 global reanalysis. *Quarterly Journal of the Royal Meteorological Society*, 146(730), 1999–2049. Retrieved from <https://doi.org/10.1002/qj.3803>
- Howat, I. (2017a). *MEaSUREs Greenland Ice Mapping Project (GIMP) 2000 Image Mosaic, Version 1*. NASA National Snow and Ice Data Center Distributed Active Archive Center. Retrieved from <https://doi.org/10.5067/4RNTRE4JCYD>
- Howat, I. (2017b). *MEaSUREs greenland ice mapping project (GIMP) land ice and ocean classification mask, version 1 [data set]*. 'NASA National Snow and Ice Data Center Distributed Active Archive Center'. Retrieved from <https://doi.org/10.5067/B8X58MQBFUPA>
- Howat, I., Negrete, A., & Smith, B. (2022). *Digital Elevation Model from GeoEye and WorldView Imagery, Version 2 [Data Set]*. 'NASA National Snow and Ice Data Center Distributed Active Archive Center'. Retrieved from <https://doi.org/10.5067/BHS4S5GAMFVY>
- Howat, I. M., Negrete, A., & Smith, B. E. (2014). The greenland ice mapping project (GIMP) land classification and surface elevation data sets. *The Cryosphere*, 8(4), 1509–1518. Retrieved from <https://doi.org/10.5194/tc-8-1509-2014>
- Howell, S. E., Small, D., Rohner, C., Mahmud, M. S., Yackel, J. J., & Brady, M. (2019). Estimating melt onset over Arctic sea ice from time series multi-sensor Sentinel-1 and RADARSAT-2 backscatter. *Remote Sensing of Environment*, 229, 48–59. Retrieved from <https://doi.org/10.1016/j.rse.2019.04.031>
- Iakubovskii, P. (2023). *segmentation models pytorch*. github. Retrieved from [https://github.com/qubvel/segmentation\\_models.pytorch](https://github.com/qubvel/segmentation_models.pytorch) (last accessed 05/2024)
- Isensee, F., Jaeger, P. F., Kohl, S. A. A., Petersen, J., & Maier-Hein, K. H. (2021). nnU-Net: a self-configuring method for deep learning-based biomedical image segmentation. *Nature Methods*, 18(2), 203-211. Retrieved from <https://doi.org/10.1038/s41592-020-01008-z>
- Isola, P., Zhu, J.-Y., Zhou, T., & Efros, A. A. (2017). Image-to-Image Translation with Conditional Adversarial Networks. In *2017 IEEE Conference on Computer Vision and Pattern Recognition (CVPR)* (p. 5967-5976). Retrieved from <https://doi.org/10.1109/CVPR.2017.632>

- Jakubik, J., Yang, F., Blumenstiel, B., Scheurer, E., Sedona, R., Maurogiovanni, S., ... Longépé, N. (2025). *TerraMind: Large-Scale Generative Multimodality for Earth Observation*. arXiv. Retrieved from <https://arxiv.org/abs/2504.11171>
- Johnson, A., Fahnstock, M., & Hock, R. (2020). Evaluation of passive microwave melt detection methods on Antarctic Peninsula ice shelves using time series of Sentinel-1 SAR. *Remote Sensing of Environment*, 250, 112044. Retrieved from <https://doi.org/10.1016/j.rse.2020.112044>
- Karras, T., Aila, T., Laine, S., & Lehtinen, J. (2018). Progressive growing of GANs for improved quality, stability, and variation. In *International conference on learning representations*. Retrieved from <https://openreview.net/forum?id=Hk99zCeAb>
- Kittel, C., Fettweis, X., Picard, G., & Gourmelen, N. (2022). Assimilation of satellite-derived melt extent increases melt simulated by MAR over the Amundsen sector (West Antarctica). *Bulletin de la Société Géographique de Liège*, 78, 87–99. Retrieved from <https://doi.org/10.25518/0770-7576.6616>
- Klemmer, K., Rolf, E., Robinson, C., Mackey, L., & Rußwurm, M. (2025). SatCLIP: Global, General-Purpose Location Embeddings with Satellite Imagery. *Proceedings of the AAAI Conference on Artificial Intelligence*, 39(4), 4347–4355. Retrieved from <https://doi.org/10.1609/aaai.v39i4.32457>
- Kurinchi-Vendhan, R., Lütjens, B., Gupta, R., Werner, L. D., Newman, D., & Low, S. (2021). WiSoSuper: Benchmarking Super-Resolution Methods on Wind and Solar Data. In *Neurips 2021 workshop on tackling climate change with machine learning*. Retrieved from <https://www.climatechange.ai/papers/neurips2021/17>
- Lacoste, A., Lehmann, N., Rodriguez, P., Sherwin, E., Kerner, H., Lütjens, B., ... Zhu, X. (2023). GEO-Bench: Toward Foundation Models for Earth Monitoring. In *Advances in neural information processing systems* (Vol. 36, pp. 51080–51093). Retrieved from <https://dl.acm.org/doi/10.5555/3666122.3668345>
- Langguth, M., Harder, P., Schicker, I., Patnala, A., Lehner, S., Mayer, K., & Dabernig, M. (2024). A benchmark dataset for meteorological downscaling. *ICLR Workshop on Tackling Climate Change with Machine Learning Abstract*. Retrieved from <https://doi.org/10.34734/FZJ-2024-07378>
- Levinson, J. F., Howat, I., & Tscherning, C. (2013). Improving maps of ice-sheet surface elevation change using combined laser altimeter and stereoscopic elevation model data. *Journal of Glaciology*, 59(215), 524–532. Retrieved from <https://doi.org/10.3189/2013JoG12J114>
- Li, H., Yang, Y., Chang, M., Chen, S., Feng, H., Xu, Z., ... Chen, Y. (2022). Srdiff: Single image super-resolution with diffusion probabilistic models. *Neurocomputing*, 479, 47–59. Retrieved from <https://doi.org/10.1016/j.neucom.2022.01.029>
- Lindsey, R. (2022, September 23). *Unusually large, late melt spike on Greenland in September 2022*. Climate.gov event tracker. Retrieved from <https://www.climate.gov/news-features/event-tracker/unusually-large-late-melt-spike-greenland-september-2022> (last accessed August 2024)
- Liu, C., & Sun, D. (2014). On Bayesian Adaptive Video Super Resolution. *IEEE Transactions on Pattern Analysis and Machine Intelligence*, 36(2), 346–360. Retrieved from <https://doi.org/10.1109/TPAMI.2013.127>
- Liu, H., Wang, L., & Jezek, K. C. (2005). Wavelet-transform based edge detection approach to derivation of snowmelt onset, end and duration from satellite passive microwave measurements. *International Journal of Remote Sensing*, 26(21), 4639–4660. Retrieved from <https://doi.org/10.1080/01431160500213342>
- Loos, V., Pardasani, R., & Awasthi, N. (2024). *Demystifying the Effect of Receptive Field Size in U-Net Models for Medical Image Segmentation*. arXiv. Retrieved from <https://arxiv.org/abs/2406.16701>
- Loshchilov, I., & Hutter, F. (2017). SGDR: Stochastic gradient descent with warm restarts. In *International conference on learning representations*. Retrieved from <https://openreview.net/forum?id=Skq89Scxx>



- Luckman, A., Elvidge, A., Jansen, D., Kulesa, B., Munneke, P. K., King, J., & Barrand, N. E. (2014). Surface melt and ponding on larsen c ice shelf and the impact of föhn winds. *Antarctic Science*, 26(6), 625–635. Retrieved from <https://doi.org/10.1017/S0954102014000339>
- Lütjens, B., Ferrari, R., Watson-Parris, D., & Selin, N. E. (2025). The impact of internal variability on benchmarking deep learning climate emulators. *Journal of Advances in Modeling Earth Systems*, 17(8). Retrieved from <https://doi.org/10.1029/2024MS004619>
- Lütjens, B., Leshchinskiy, B., Boulais, O., Chishtie, F., Díaz-Rodríguez, N., Masson-Forsythe, M., ... Newman, D. (2024). Generating physically-consistent satellite imagery for climate visualizations. *IEEE Transactions on Geoscience and Remote Sensing*, 62, 1-11. doi: <https://doi.org/10.1109/TGRS.2024.3493763>
- Mardani, M., Brenowitz, N., Cohen, Y., Pathak, J., Chen, C.-Y., Liu, C.-C., ... Pritchard, M. (2025). Residual corrective diffusion modeling for km-scale atmospheric downscaling. *Communications Earth & Environment*, 6(1), 124. Retrieved from <https://doi.org/10.1038/s43247-025-02042-5>
- Marsocci, V., Jia, Y., Bellier, G. L., Kerekes, D., Zeng, L., Hafner, S., ... Nascetti, A. (2024). PANGAEA: A Global and Inclusive Benchmark for Geospatial Foundation Models. arXiv. Retrieved from <https://arxiv.org/abs/2412.04204>
- Mattingly, K. S., Mote, T. L., & Fettweis, X. (2018). Atmospheric river impacts on greenland ice sheet surface mass balance. *Journal of Geophysical Research: Atmospheres*, 123(16), 8538-8560. Retrieved from <https://doi.org/10.1029/2018JD028714>
- Mattingly, K. S., Turton, J. V., Wille, J. D., Noël, B., Fettweis, X., Rennermalm, Å. K., & Mote, T. L. (2023). Increasing extreme melt in northeast Greenland linked to foehn winds and atmospheric rivers. *Nature Communications*, 14(1), 1743. Retrieved from <https://doi.org/10.1038/s41467-023-37434-8>
- McMillan, M., Leeson, A., Shepherd, A., Briggs, K., Armitage, T. W. K., Hogg, A., ... Gilbert, L. (2016). A high-resolution record of greenland mass balance. *Geophysical Research Letters*, 43(13), 7002-7010. Retrieved from <https://doi.org/10.1002/2016GL069666>
- Meier, W. N., & Stewart, J. S. (2020a). Assessing the potential of enhanced resolution gridded passive microwave brightness temperatures for retrieval of sea ice parameters. *Remote Sensing*, 12(16). Retrieved from <https://doi.org/10.3390/rs12162552>
- Meier, W. N., & Stewart, J. S. (2020b). Assessment of the stability of passive microwave brightness temperatures for nasa team sea ice concentration retrievals. *Remote Sensing*, 12(14). Retrieved from <https://doi.org/10.3390/rs12142197>
- Miles, K. E., Willis, I. C., Benedek, C. L., Williamson, A. G., & Tedesco, M. (2017). Toward Monitoring Surface and Subsurface Lakes on the Greenland Ice Sheet Using Sentinel-1 SAR and Landsat-8 OLI Imagery. *Frontiers in Earth Science*, 5. Retrieved from <https://doi.org/10.3389/feart.2017.00058>
- Mioduszewski, J., Rennermalm, A. K., Hammann, A., Tedesco, M., Noble, E. U., Stroeve, J. C., & Mote, T. L. (2016). Atmospheric drivers of Greenland surface melt revealed by self-organizing maps. *Journal of Geophysical Research: Atmospheres*, 121(10), 5095–5114. Retrieved from <https://doi.org/10.1002/2015JD024550>
- Moon, T. A., Tedesco, M., Box, J. E., Cappelen, J., Fausto, R. S., Fettweis, X., ... Winton, Ø. A. (2021). *Arctic Report Card 2021: Greenland Ice Sheet*. Retrieved from <https://doi.org/10.25923/546g-ms61> (NOAA Technical Report)
- National Snow and Ice Data Center. (2022). *MEaSUREs greenland ice mapping project (GrIMP) digital elevation model from GeoEye and WorldView imagery, version 2*. Retrieved from <https://nsidc.org/sites/default/files/documents/user-guide/nsidc-0715-v002-userguide.pdf>
- Noël, B., van de Berg, W. J., Lhermitte, S., Wouters, B., Machguth, H., Howat, I., ... van den Broeke, M. R. (2017). A tipping point in refreezing accelerates mass loss of Greenland's glaciers and ice caps. *Nature Communications*, 8(1), 14730. Retrieved from <https://doi.org/10.1038/ncomms14730>



- Noël, B., van de Berg, W. J., Machguth, H., Lhermitte, S., Howat, I., Fettweis, X., & van den Broeke, M. R. (2016). A daily, 1 km resolution data set of downscaled greenland ice sheet surface mass balance (1958–2015). *The Cryosphere*, 10(5), 2361–2377. Retrieved from <https://doi.org/10.5194/tc-10-2361-2016>
- Rasp, S., Dueben, P. D., Scher, S., Weyn, J. A., Mouatadid, S., & Thuerey, N. (2020). Weatherbench: A benchmark data set for data-driven weather forecasting. *Journal of Advances in Modeling Earth Systems*, 12(11), e2020MS002203. Retrieved from <https://doi.org/10.1029/2020MS002203>
- Rolf, E., Klemmer, K., Robinson, C., & Kerner, H. (2024). Position: mission critical - satellite data is a distinct modality in machine learning. In *Proceedings of the 41st international conference on machine learning*. JMLR.org. Retrieved from <https://dl.acm.org/doi/10.5555/3692070.3693807>
- Ronneberger, O., Fischer, P., & Brox, T. (2015). U-net: Convolutional networks for biomedical image segmentation. In *Medical image computing and computer-assisted intervention – miccai 2015* (pp. 234–241). Springer International Publishing. Retrieved from [https://doi.org/10.1007/978-3-319-24574-4\\_28](https://doi.org/10.1007/978-3-319-24574-4_28)
- Rouault, E., Warmerdam, F., Schwehr, K., Kiselev, A., Butler, H., Loskot, M., . . . Miura, H. (2024). *Gdal*. Zenodo. Retrieved from <https://doi.org/10.5281/zenodo.11175199>
- Ryan, J. C. (2024). Contribution of surface and cloud radiative feedbacks to Greenland Ice Sheet meltwater production during 2002–2023. *Communications Earth & Environment*, 5(1), 538. Retrieved from <https://doi.org/10.1038/s43247-024-01714-y>
- Saharia, C., Ho, J., Chan, W., Salimans, T., Fleet, D. J., & Norouzi, M. (2023). Image Super-Resolution via Iterative Refinement. *IEEE Transactions on Pattern Analysis and Machine Intelligence*, 45(4), 4713–4726. Retrieved from <https://doi.org/10.1109/TPAMI.2022.3204461>
- Scher, C., Steiner, N. C., & McDonald, K. C. (2021). Mapping seasonal glacier melt across the Hindu Kush Himalaya with time series synthetic aperture radar (SAR). *The cryosphere*, 15(9), 4465–4482. Retrieved from <https://doi.org/10.5194/tc-15-4465-2021>
- Sha, Y., II, D. J. G., West, G., & Stull, R. (2020). Deep-learning-based gridded downscaling of surface meteorological variables in complex terrain. part i: Daily maximum and minimum 2-m temperature. *Journal of Applied Meteorology and Climatology*, 59(12), 2057 – 2073. Retrieved from <https://doi.org/10.1175/JAMC-D-20-0057.1>
- Shimada, R., Takeuchi, N., & Aoki, T. (2016). Inter-annual and geographical variations in the extent of bare ice and dark ice on the Greenland ice sheet derived from MODIS satellite images. *Frontiers in Earth Science*, 4, 43. Retrieved from <https://doi.org/10.3389/feart.2016.00043>
- Stengel, K., Glaws, A., Hettinger, D., & King, R. N. (2020). Adversarial super-resolution of climatological wind and solar data. *Proceedings of the National Academy of Sciences*, 117(29), 16805–16815. Retrieved from <https://doi.org/10.1073/pnas.1918964117>
- Stevens, L. A., Nettles, M., Davis, J. L., Creyts, T. T., Kingslake, J., Ahlstrøm, A. P., & Larsen, T. B. (2022). Helheim Glacier diurnal velocity fluctuations driven by surface melt forcing. *Journal of Glaciology*, 68(267), 77–89. Retrieved from <https://doi.org/10.1017/jog.2021.74>
- Stiles, W. H., & Ulaby, F. T. (1980). The active and passive microwave response to snow parameters: 1. Wetness. *Journal of Geophysical Research: Oceans*, 85(C2), 1037–1044. Retrieved from <https://doi.org/10.1029/JC085iC02p01037>
- Subich, C., Husain, S. Z., Separovic, L., & Yang, J. (2025). Fixing the Double Penalty in Data-Driven Weather Forecasting Through a Modified Spherical Harmonic Loss Function. In *Forty-second international conference on machine learning*. Retrieved from <https://openreview.net/forum?id=YNh770LRid>
- Tedesco, M. (2007). Snowmelt detection over the Greenland ice sheet from SSM/I brightness temperature daily variations. *Geophysical Research Letters*, 34(2). Retrieved from <https://doi.org/10.1029/2006GL028466>

- Tedesco, M. (2009). Assessment and development of snowmelt retrieval algorithms over Antarctica from K-band spaceborne brightness temperature (1979–2008). *Remote Sensing of Environment*, 113(5), 979–997. Retrieved from <https://doi.org/10.1016/j.rse.2009.01.009>
- Tedesco, M., Brodzik, M., Armstrong, R., Savoie, M., & Ramage, J. (2009). Pan arctic terrestrial snowmelt trends (1979–2008) from spaceborne passive microwave data and correlation with the arctic oscillation. *Geophysical Research Letters*, 36(21). Retrieved from <https://doi.org/10.1029/2009GL039672>
- Tedesco, M., Colosio, P., Fettweis, X., & Cervone, G. (2023). A computationally efficient statistically downscaled 100 m resolution greenland product from the regional climate model mar. *The Cryosphere*, 17(12), 5061–5074. Retrieved from <https://doi.org/10.5194/tc-17-5061-2023>
- Tedesco, M., & Fettweis, X. (2020). Unprecedented atmospheric conditions (1948–2019) drive the 2019 exceptional melting season over the Greenland ice sheet. *The Cryosphere*, 14(4), 1209–1223. Retrieved from <https://doi.org/10.5194/tc-14-1209-2020>
- tf datasets. (2024). *TensorFlow Datasets*. Retrieved from <https://www.tensorflow.org/datasets/catalog/overview> (last accessed 10/2024)
- The MathWorks Inc. (2021). *Matlab version: 9.10.0 (r2021a)*. Natick, Massachusetts, United States: The MathWorks Inc.
- Torres, R., Navas-Traver, I., Bibby, D., Lokas, S., Snoeij, P., Rommen, B., ... Geudtner, D. (2017). Sentinel-1 SAR system and mission. In *2017 IEEE Radar Conference (RadarConf)* (p. 1582-1585). Retrieved from <https://doi.org/10.1109/RADAR.2017.7944460>
- Torres, R., Snoeij, P., Geudtner, D., Bibby, D., Davidson, M., Attema, E., ... Rostan, F. (2012). GMES sentinel-1 mission. *Remote Sensing of Environment*, 120, 9-24. Retrieved from <https://doi.org/10.1016/j.rse.2011.05.028> (The Sentinel Missions - New Opportunities for Science)
- van de Berg, W. J., van Meijgaard, E., & van Ulft, L. H. (2020). The added value of high resolution in estimating the surface mass balance in southern greenland. *The Cryosphere*, 14(6), 1809–1827. Retrieved from <https://doi.org/10.5194/tc-14-1809-2020>
- van den Broeke, M. R., Kuipers Munneke, P., Noël, B., Reijmer, C., Smeets, P., van de Berg, W. J., & van Wessem, J. M. (2023). Contrasting current and future surface melt rates on the ice sheets of Greenland and Antarctica: Lessons from in situ observations and climate models. *PLOS Climate*, 2(5), 1-17. Retrieved from <https://doi.org/10.1371/journal.pclm.0000203>
- Veci, L. (2016, updated 2020). SNAP Command Line Tutorial [Computer software manual]. Retrieved from [https://step.esa.int/docs/tutorials/SNAP\\_CommandLine\\_Tutorial.pdf](https://step.esa.int/docs/tutorials/SNAP_CommandLine_Tutorial.pdf)
- Wang, T.-C., Liu, M.-Y., Zhu, J.-Y., Tao, A., Kautz, J., & Catanzaro, B. (2018, June). High-resolution image synthesis and semantic manipulation with conditional gans. In *Proceedings of the IEEE conference on computer vision and pattern recognition (cvpr)*. Retrieved from <https://arxiv.org/abs/1711.11585>
- Williams, J. J., Gourmelen, N., Nienow, P., Bunce, C., & Slater, D. (2021). Helheim Glacier poised for dramatic retreat. *Geophysical Research Letters*, 48(23). Retrieved from <https://doi.org/10.1029/2021GL094546>
- Wismann, V. (2000). Monitoring of seasonal snowmelt on Greenland with ERS scatterometer data. *IEEE Transactions on Geoscience and Remote Sensing*, 38(4), 1821–1826. Retrieved from <https://doi.org/10.1109/36.851766>
- Wolters, P., Bastani, F., & Kembhavi, A. (2023). *Zooming Out on Zooming In: Advancing Super-Resolution for Remote Sensing*. arXiv. Retrieved from <https://arxiv.org/abs/2311.18082>
- Yu, F., Seff, A., Zhang, Y., Song, S., Funkhouser, T., & Xiao, J. (2016). *LSUN: Construction of a large-scale image dataset using deep learning with humans in the loop*. arXiv. Retrieved from <https://arxiv.org/abs/1506.03365>
- Zhu, X. X., Xiong, Z., Wang, Y., Stewart, A. J., Heidler, K., Wang, Y., ... Shi, Y. (2024).

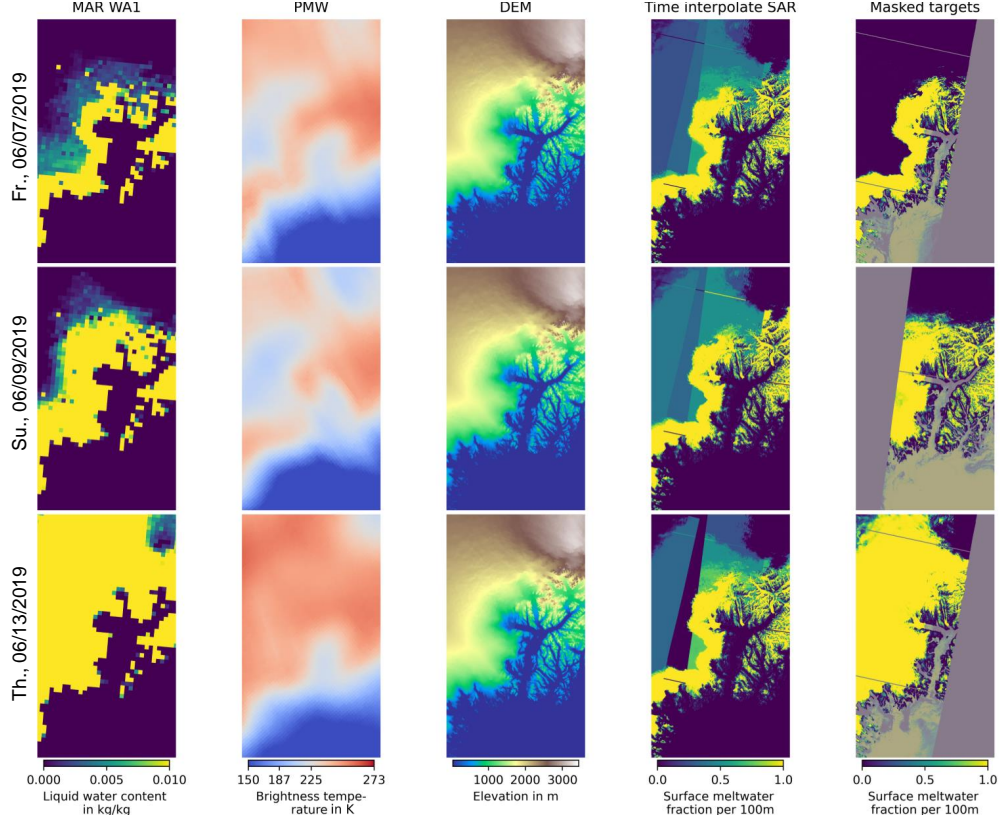


Figure A1: Input data streams (left 4 columns) and target meltwater observations (right) during the 12th of June 2019 melt event. While the target observations have a revisit time of 1-12 days and contain significant masked areas, the input datastreams are available every day at every pixel.

*On the Foundations of Earth and Climate Foundation Models.* arXiv. Retrieved from <https://arxiv.org/abs/2405.04285>

## Appendix A Additional information on data

Figure A1 shows the input data streams for the melt event on the 12th of June, 2019.

### A1 Synthetic Aperture Radar (SAR) data

For reproducibility, we provide additional details on SAR processing here and depict our workflow in Fig. A2. The initial set of processing steps involved processing of raw level-1 data using the ESA Sentinel Application Platform (SNAP) graph processing (gpt) command line software (Veci, 2016, updated 2020). The SNAP processing involved utilizing built-in functions for orbital correction (with polynomial degree 3), subsetting within the domain of interest, border noise removal (with a border margin limit of 1500 pixels and threshold value of 0.5), radiometric calibration, speckle filtering (using a Lee Sigma filter with window size 7x7, sigma of 0.9, and target window size of 3x3), terrain correction, and conversion from linear to dB scale. These are standard procedures for processing SAR data (Filipponi, 2019) and the parameters chosen were default values with the exception of the terrain correction

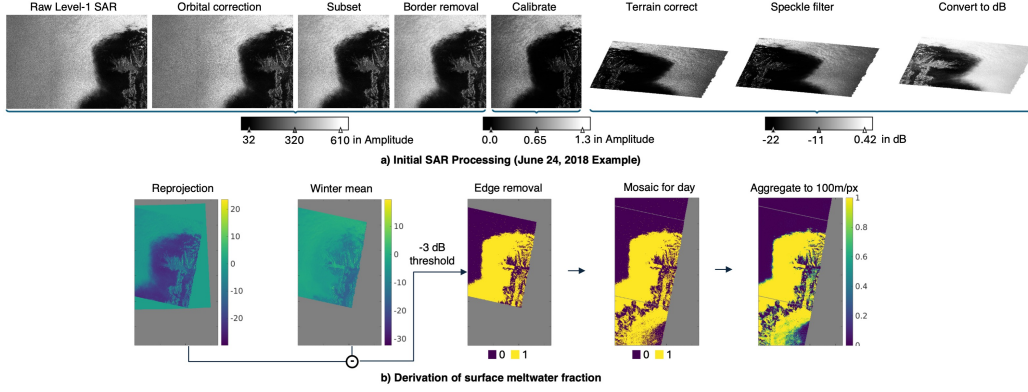


Figure A2: **Deriving meltwater targets from SAR.** We preprocess SAR Level-1 data following the steps in (a). Then, we reproject and convert SAR backscattering intensity into surface meltwater fraction per 100m grid cell (b).

step and the border margin limit for border noise removal, which was increased to 1500 from 500 after testing on our input data. For the terrain correction step we utilized the 30m-resolved DEM, described in Section 2.2.4. We reprojected the data onto a 10m equal area grid using bilinear interpolation.

During the final processing steps performed using MATLAB (The MathWorks Inc., 2021), we computed and subtract the previous year’s per-pixel winter mean backscatter (Dec, Jan, Feb) from each 10m-resolved SAR scene and thresholded the data at -3dB such that any value below -3dB relative to the winter mean was considered to be melting. In order to ensure that variations in satellite orbit, viewing geometry, or data collection time did not introduce errors in the dataset, we only compared data for a given scene with winter data collected with the same orbital geometry. To ensure this, we grouped summer and winter data for a given year according to measurements collected at the satellite repeat time interval of 12 days. This was done by looping through files within the dataset and finding files within 12 days  $\pm$  4 seconds from the previous file. Following this procedure all winter files within a given group were averaged, and subtracted from the summer files within the same group to compute melting for a given summer image.

The initial processing steps were applied to  $\sim$ 3000 observations. After computing melt, files were visually examined, revealing the persistence of some edge artifacts with apparently anomalous melting along the borders of the data swath in some images. This likely resulted from imperfections in the various corrections (i.e. terrain correction, orbital correction, and border noise removal) conducted for the original SAR data. To remove this spurious data, we removed the borders for computed melt data using the following method:

1. A binary mask was created to separate valid vs. missing data for the image.
2. The canny edge detection method was applied to find the borders of valid data within the image using MATLAB software.
3. The edges were expanded using the “diag” and “thicken” functions.
4. Thickening was performed until a visual examination revealed that the edge artifacts had been removed.

Following edge removal, all images from a given day were mosaicked using MATLAB to produce 10m resolution melt masks for individual days. In the case of overlap between images, if any of the images showed melt for a given pixel, that pixel was classified as melting. Melt data on the 10m grid were then aggregated onto the common 100m grid by

computing the fraction of 10m grid cells exhibiting melt within each 100m grid cell. The 10m grid was chosen to be a subset of the 100m grid. The 100m fractional melt dataset was then used within the experiments for training and validation purposes.

## A2 Passive Microwave (PMW) data

We utilized enhanced resolution PMW data in the 37 GHz channel from the Special Sensor Microwave Imager/Sounder (SSMIS) sensor onboard the Defense Meteorological Satellite Program (DMSP) F17 satellite, available twice daily (with a morning and evening pass) at a spatial resolution of 3.125 km through the MEaSUREs program, distributed by the National Snow and Ice Data Center (NSIDC) (Brodzik et al., 2016). de Roda Husman et al. (2024a) uses the analogous 6.25km SSMIS product from the same source. We restrict our dataset to the evening pass ( $\approx 18:30$  local solar time (Meier & Stewart, 2020b)) for consistency. The standard resolution for distributing PMW data is 25 km, obtained using a drop-in-the bucket method where multiple PMW measurements falling within a grid cell on a polar stereographic grid for a given day are averaged (Meier & Stewart, 2020a). The enhanced resolution product (Meier & Stewart, 2020a) differs in that it provides a local measurement for morning and evening passes on an equal area grid, and enhances the spatial resolution by utilizing a different signal processing method in which information about the sensor measurement response function for measurements overlapping in space at a given overpass time is used to synthesize a higher resolution signal, enabling a higher level of detail in Greenland melt estimates (Colosio et al., 2020). Despite the higher resolution grid, the effective resolution associated with the smallest resolvable feature is lower (between 3.125 and 25 km) given that a smoothing function is applied during processing (Meier & Stewart, 2020a).

For our study, PMW data were obtained in the form of netcdf files from the NSIDC access tool. To produce the input dataset, raw netcdf files were converted to geotiff format using a shell script and the gdal-translate command line tool (Rouault et al., 2024). Finally, the geotiffs were reprojected to the Albers equal area 100m grid over the Helheim Glacier region using the gdalwarp command and nearest-neighbor interpolation.

This dataset along with other PMW data were used recently to produce a high-resolution record of Greenland ice sheet melt covering the period 1979-2019 using a threshold-based approach (Colosio et al., 2020).

If a PMW observation of a given day contains any missing values, we exclude this day from our train, val, and test datasets. A total of 35 images for which matching SAR observations are present were eliminated from the analysis. Our auxiliary dataset contains all data between Jan. 1, 2016 and Dec. 31, 2023 to be able to calculate the winter means that are needed for common PMW-based downscaling methods (see Section 2.6.1).

## A3 MAR regional climate model (RCM) data

The MAR data is distributed in the form of yearly netcdf files containing daily average model output. While we downloaded daily average output, data would also be available for download as temporal snapshots. A subset of variables, detailed in Table A1 were extracted from the raw data using netcdf Operators (NCO) software. The netcdf data were then converted to geotiff format and reprojected to the 100m equal area grid using gdal software and nearest-neighbor interpolation as was done for the PMW data.

The auxiliary variables in Table A1 could add information, such as heatwaves, heavy rainfall, higher humidity, and sunny days (as indicated by high SWD) that can accelerate melting (Hermann et al., 2020; Tedesco & Fettweis, 2020; Antwerpen et al., 2022; Ryan, 2024). Low temperatures and high winds can accelerate refreezing. The auxiliary variables might also enable insight into larger spatial patterns (Mioduszewski et al., 2016; Mattingly et



Table A1: MAR data overview. Overview of all data variables in our auxiliary input dataset from MARv3.14. The core dataset contains daily averaged liquid water content within the top meter of snow (WA1) at 5km spatial resolution.

Variable	abbr	unit	Variable	abbr	unit
average liquid water content within the top meter of snow	WA1	kg/kg	surface albedo	AL2	-
surface air temperature (2m above sfc.)	TTZ	°C	cloud optical depth	COD	-
specific humidity (2m above sfc.)	QQZ	g/kg	lower atmosphere cloud fraction	CD	-
y-direction ( northward) 2m wind speed	V2Z	m/s	middle atmosphere cloud fraction	CM	-
x-direction ( eastward) wind speed	U2Z	m/s	upper atmosphere cloud fraction	CU	-
rainfall	RF	mm/day	latent heat flux	LHF	W/m <sup>2</sup>
snowfall (in water equivalent units)	SF	mm/day	sensible heat flux	SHF	W/m <sup>2</sup>
melt	ME	mm/day	surface atmospheric pressure	SP	hPa
surface mass balance (in water equivalent units)	SMB	mm/day	shortwave downward welling radiation	SWD	W/m <sup>2</sup>
			longwave downward welling radiation	LWD	W/m <sup>2</sup>

al., 2018), such as a high pressure area over southeasternmost Greenland and could indicate clockwise winds over Greenland that pull warm air from lower latitudes (Lindsey, 2022).

The MARv3.14 model domain encompasses the Greenland ice sheet as illustrated in Fig. 2. MAR simulates surface and atmospheric processes within this regional domain while being forced with ERA5 data at the lateral and ocean surface boundaries. MAR has been used in several studies of Greenland surface processes (Fettweis et al., 2017; Antwerpen et al., 2022; Delhasse et al., 2024).

#### A4 Digital elevation model (DEM) data

As an additional input to the models discussed below, we used the Greenland Ice sheet Mapping Project (GrIMP) v2.0 digital elevation model (DEM) mosaic of the ice sheet surface topography, available at a 30m spatial resolution (I. Howat et al., 2022; I. M. Howat et al., 2014). The product is derived from panchromatic stereoscopic imagery collected by the Maxar GeoEye-1, WorldView-1,-2, and -3 satellites, collected over the May 2008 through November 2020 period, and registered to ICESat-2 ATL06 lidar-derived elevations collected in the summers of 2019 and 2020 using the co-registration procedure of (Levinson et al., 2013) (National Snow and Ice Data Center, 2022). The product is distributed as a set of 36 tiles covering the Greenland ice sheet, distributed in Geotiff format. To produce the DEM used as part of our analysis, we utilized the gdalwarp tool to mosaic the GrIMP tiles covering our study area, reproject them to the 10m resolution sub-grid of the common 100m resolution grid over the Helheim region, and then average the 10m data onto the common 100m resolution grid.

#### A5 Land-ocean mask

A similar procedure was conducted on the GIMP (earlier acronym for GrIMP) land-ocean mask (I. Howat, 2017b; I. M. Howat et al., 2014). The GIMP land-ocean mask was mapped using a combination of USGS Landsat 7 ETM+ panchromatic band and the RADARSAT-1 SAR images from the Canadian Space Agency. The mask is provided in GeoTIFF format similarly to the GrIMP DEM, at a 15, 30 or 90m spatial resolution. We chose the 30m data to be consistent with the DEM. As for the DEM, we used the gdalwarp tool to mosaic tiles overlapping with our study area, reprojected the data onto the 100m sub-grid, and averaged the mask onto the common 100m resolution grid.

#### A6 Additional information on data statistics and split

We excluded the last month within our study period (Sep 2023) from the core dataset because MAR data was only available until Aug 31, 2023.



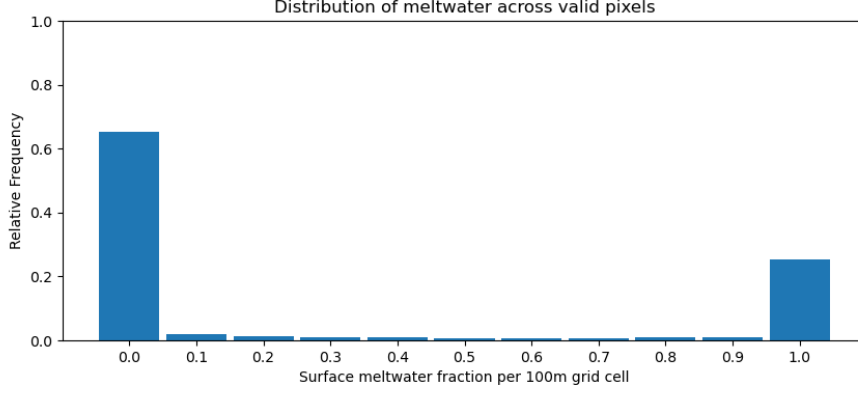


Figure A3: Histogram of the surface meltwater targets across the training dataset. The targets are in the set of real numbers in  $[0, 1]$  and are displayed as a binned distribution ( $n = 11$ ) normalized to relative frequency. The targets are slightly imbalanced towards no-melt pixels (no-melt:melt = 65.4% : 34.6%), considering only valid pixels over land, and assuming a cut-off for binary classification at 0.10.

Figure A3 shows the distribution of surface meltwater across the training dataset.

Figure A4a shows the total number of observed days per month and Fig. A4b shows the observed pixels in % of the total image per day across the entire dataset.

Our core dataset is arguably small-to-medium sized in comparison to common super-resolution datasets: The total number of pixels (valid and invalid) in our dataset is equivalent to  $\approx 2,400$  images at 1K resolution, i.e.,  $(1024 \times 1024)$  pixels, which are less pixels than in the 1000 DIV2K images at  $\approx 2K$  resolution, 30,000 CelebA-HQ images at 1K resolution, or 10-60 million LSUN images at 0.25K resolution (Agustsson & Timofte, 2017; Karras et al., 2018; Yu et al., 2016). In comparison to the  $\sim 20GB$  of our core dataset, DIV2K-default measures  $\sim 4.7GB$ , CelebA-HQ-1k  $\sim 54GB$ , and LSUN-total  $\sim 1.1TB$  (tf datasets, 2024).

We reject the year 2017 from the validation and test sets. Figure A4a shows that the dataset contains 10-23 observations per month, except for 2017 which only records 2-4 monthly observations. Furthermore, all images in 2017 are only valid over the southwest of the glacier. Thus, we cannot robustly evaluate the accuracy of a model over the full study area for 2017. We keep the 2017 data in the training set to have additional training samples.

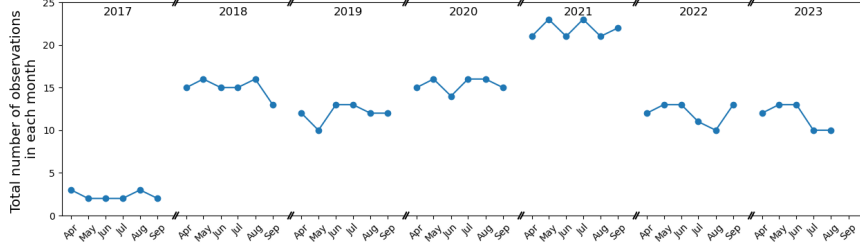
**R-squared.** We calculate the R-squared,  $R^2$ , due to its common use. The R-squared is related to the MSE through a normalization factor proportional to a measure of dispersion and a rescaling to  $[-\infty, 1]$  – with 1 as the best value.

## Appendix B Additional information on metrics and models

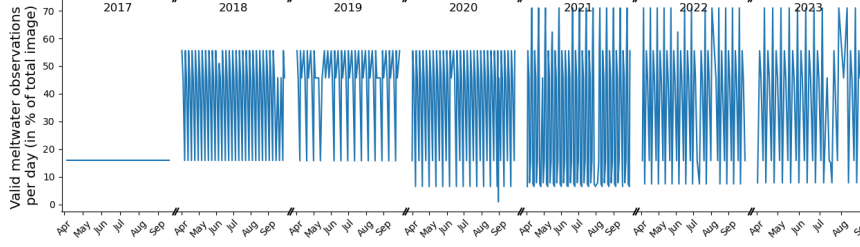
### B1 Appendix to Evaluation Metrics

The precision and recall are calculated as follows.

$$\text{Prec}(\mathbf{Y}, \hat{\mathbf{Y}}) = \frac{1}{N_{\text{valid}}} \sum_k^K n_{\text{valid},k} \frac{\sum_{(i,j) \in IJ_{\text{valid},k}} \mathbb{1}(y_{k,i,j} > y_{\text{thold}}) \mathbb{1}(\hat{y}_{k,i,j} > y_{\text{thold}})}{\sum_{(i,j) \in IJ_{\text{valid},k}} \mathbb{1}(\hat{y}_{k,i,j} > y_{\text{thold}})} \quad (\text{B1})$$



(a) Total number of observed days per month. We count a day as observed if all core input and target data streams are available. Starting in 2022, data from S1B is unavailable.



(b) Valid target pixels per day as percentage of all pixels in the full-scale image. A target pixel is considered valid if the SAR-derived surface meltwater fraction at this pixel has been observed and has not been masked by the land-ocean mask or processing artifacts. On most days  $\approx 5, 15, 45, 55$ , or  $70\%$  of pixels are valid which corresponds to the S1A&-B swath paths that are intersecting with our study area. The plot shows all images in the core dataset.

Figure A4: Additional statistics of the observed target meltwater fraction from SAR. During 2017, only a single satellite retrieval path overlaps with our study area (bottom), resulting in few observations (top).

$$\text{Rec}(\mathbf{Y}, \hat{\mathbf{Y}}) = \frac{1}{N_{\text{valid}}} \sum_k^K n_{\text{valid},k} \frac{\sum_{(i,j) \in IJ_{\text{valid},k}} \mathbb{1}(y_{k,i,j} > y_{\text{thold}}) \mathbb{1}(\hat{y}_{k,i,j} > y_{\text{thold}})}{\sum_{(i,j) \in IJ_{\text{valid},k}} \mathbb{1}(y_{k,i,j} > y_{\text{thold}})} \quad (\text{B2})$$

The F1-score is the harmonic mean of the computed precision and recall values:

$$\text{F1}(\mathbf{Y}, \hat{\mathbf{Y}}) = \frac{2}{\frac{1}{\text{Prec}(\mathbf{Y}, \hat{\mathbf{Y}})} + \frac{1}{\text{Rec}(\mathbf{Y}, \hat{\mathbf{Y}})}} \quad (\text{B3})$$

**R-squared.** We calculate the  $R^2$  score for a set of masked image tiles as follows:

$$R^2(\mathbf{Y}, \hat{\mathbf{Y}}) = \frac{1}{N_{\text{valid}}} \sum_k^K n_{\text{valid},k} \max \left( -1, \left( 1 - \frac{\sum_{(i,j) \in IJ_{\text{valid},k}} (y_{k,i,j} - \hat{y}_{k,i,j})^2}{\sum_{(i,j) \in IJ_{\text{valid},k}} (y_{k,i,j} - \bar{y}_k)^2} \right) \right) \quad (\text{B4})$$

where the  $\max(\cdot)$  term calculates the  $R^2$  of tile  $k$  and clips the  $R^2$  of each tile  $k$  to  $[-1, 1]$  to avoid large negative outliers that would skew the mean. The  $n_{\text{valid},k}$  term reweights the value, such that, each valid pixel is given the same weight across all tiles;  $\bar{y}_k$  is the mean over the target tile,  $\bar{y}_k = \frac{1}{|IJ_{\text{valid},k}|} \sum_{(i,j) \in IJ_{\text{valid},k}} y_{k,i,j}$ . If all pixels in the image tile are invalid, the  $R^2$  of that tile is zero.

### B2 Model set-up: Running mean SAR

The running mean SAR model forecasts every pixel to take the average values of the  $k_h$  meltwater observations in the training set before and after at that location. If the prior or posterior image pixel is masked then the image value is not considered. This leads to a model that calculates the target value as:

$$\hat{y}_{k,i,j} = \frac{\sum_{k' \in K_k} \mathbb{1}\{(i,j) \in IJ_{\text{valid},k'}\} y_{k',i,j}}{\sum_{k' \in K_k} \mathbb{1}\{(i,j) \in IJ_{\text{valid},k'}\}} \quad (\text{B5})$$

where  $\hat{y}_{k,i,j}$  is the predicted pixel value for the  $k$ -th image at location  $(i,j)$ ;  $K_k = \{k - k_h, \dots, k - 1, k + 1, \dots, k + k_h\}$  is the set of image indices  $k_h$  steps before and after the index  $k$ ;  $\mathbb{1}\{(i,j) \in IJ_{\text{valid},k'}\}$  is 1 if the location  $(i,j)$  is in the set of valid pixels for the  $k'$ -th image and 0 otherwise;  $y_{k',i,j}$  is the pixel value of the  $k'$ -th image at location  $(i,j)$ .

We choose the interpolation horizon,  $k_h = 3$ . We treated this choice as a hyperparameter and found the best value on the validation set calculating scores for the set  $k_h \in \{1, 2, 3\}$ . With this horizon, the running mean equals a running mean over a span of 2 – 3 weeks.  $k_h = 3$  was likely the best value because it ensures that there is at least one valid pixel at every location in most predicted images, but at the same time the surrounding images are not too far away from the target image. When using this model to predict an image,  $\hat{y}$ , in the validation dataset, the input images,  $y$ , are chosen only from the training dataset. We also use this model to generate the 'running mean' inputs for the machine learning models, in which case, both  $\hat{y}$  and  $y$  are drawn from the training dataset.

### B3 Model set-up: Interpolate MAR

The interpolate MAR model smoothes out the MAR WA1 inputs using a Gaussian Blur and then readjusts the cutoff value for melt/no-melt using brightness and gamma adjustment. Finally, a landmask is applied to mask out ocean pixels. We implement each transform using pytorch and find the best parameters for each by sweeping over the values in the following ranges: Gaussian blur kernel size [91, 201], Gaussian blur standard deviation [33, 99], gamma [0.001, 30], brightness factor [40, 200].

### B4 Model set-up: Threshold PMW

The threshold PMW model follows the implementation in (Colosio et al., 2020), eq. (3), which is based on the work by (Tedesco et al., 2009). The model computes the predictions,  $\hat{y}_{k,i,j}$ , as follows:

$$\hat{y}_{k,i,j} = \begin{cases} 1, & \text{if } x_{k,i,j}^{\text{PMW}} > x_{\text{yr}_k,i,j}^{\text{PMW-Threshold}} \\ 0, & \text{otherwise} \end{cases} \quad (\text{B6})$$

$$x_{\text{yr}_k,i,j}^{\text{PMW-Threshold}} = \gamma x_{\text{yr}_k,i,j}^{\text{PMW-winter}} + \omega \quad (\text{B7})$$

$$x_{\text{yr}_k,i,j}^{\text{PMW-winter}} = \frac{1}{|\mathbb{K}_{\text{yr}_k, \text{winter}}|} \sum_{k' \in \mathbb{K}_{\text{yr}_k, \text{winter}}} x_{k',i,j}^{\text{PMW}} \quad (\text{B8})$$

where  $x_{\text{yr}_k,i,j}^{\text{PMW-Threshold}}$  is the brightness temperature threshold (in Kelvin) at location  $(i,j)$  for the year  $\text{yr}_k$  of the  $k$ -th image. The threshold is a linear function of the Winter mean brightness temperature,  $x_{\text{yr}_k,i,j}^{\text{PMW-winter}}$ , with intercept,  $\omega$ , and slope  $\gamma$  which are constants based on an electromagnetic model as detailed in (Colosio et al., 2020). The Winter mean is the average per-pixel value over all images in January and February of the corresponding year; denoted by the indices  $k' \in \mathbb{K}_{\text{yr}_k, \text{winter}}$ .

Tuning the parameters  $\gamma$  and  $\omega$  on the training dataset might result in a more accurate model for our use-case. However, we decided against tuning this model to maintain comparability with prior comparative studies, e.g., in (Colosio et al., 2020). We use the values  $\gamma = 0.48$  and  $\omega = 128K$  that are reported in (Colosio et al., 2020) which finds the best parameters across Greenland. The biases do not necessarily represent what the bias across Greenland looks like and is rather to point out possible discrepancies when zooming into one location in detail.

### B5 Model set-up: Threshold DEM

The threshold DEM model finds the best monthly linear fit and cut-off values to the DEM input. The model predictions are

$$\hat{y}_{k,i,j} = \tanh_{\text{hat}}(a_{\text{mon}_k} x_{i,j}^{\text{DEM}} + b_{\text{mon}_k}) \text{ with} \quad (\text{B9})$$

$$\tanh_{\text{hat}}(z) = 0.5 (\tanh(c + z) + \tanh(c - z)) \quad (\text{B10})$$

where  $\text{mon}_k \in \{4, \dots, 9\}$  indices the month of the  $k$ -th image,  $x_{i,j}^{\text{DEM}}$  is the DEM input at location  $(i, j)$ , and  $a_{\text{mon}_k}, b_{\text{mon}_k}$ , are parameters and  $c$  is a hyperparameter. The  $\tanh_{\text{hat}}$  is a custom activation function that resembles a boater straw hat – it is zero except for a continuous one-valued region with tanh-shaped transitions. The parameters  $a_{\text{mon}_k}$  and  $b_{\text{mon}_k}$  are independent of the year and determine the width and location of the threshold region while  $c$  determines the sharpness of zero-one transitions. The hyperparameter  $c$  is set to  $c = 4$  and the best parameters  $(a_{\text{mon}_k}, b_{\text{mon}_k})$  are found using the training and validation dataset after 22 epochs with stochastic gradient descent, batch size 16, MSE loss, initial learning rate 10, and reducing it by  $\times 0.1$  every 5 plateauing epochs. The total number of free parameters is 12 due to  $a_{\text{mon}_k}$  and  $b_{\text{mon}_k}$  each taking a different scalar value for 6 months (Apr.-Sept.).

The lower threshold value should correspond with the firn line, below which the ice and snow completely melt during the Summer leaving a surface of bare rock

### B6 Model set-up: vanilla UNet

For all deep learning model experiments we normalize each input channel to zero-mean, unit-variance. During early experiments the predictions contained sharp edges which came from the nearest-neighbor interpolation of the large-scale PMW and MAR inputs, so we smooth these inputs using a Gaussian blur filter with kernel size 45 and 99 and standard deviation of 15 and 33 pixels, respectively. We do not normalize the targets and predictions. Data is kept at float32 precision. We use a sigmoid activation in the last layer to bound the predictions to the physically-plausible range,  $[0, 1]$ .

Our vanilla UNet has 31,038,209  $\approx 31.0\text{M}$  weights occupying 120MB at float32 precision. Figure B1 illustrates the model architecture, number of layers, blocks, and features. The reported results were trained for 500 epochs, batch size 8, tile size  $h = w = 512$ , adam optimizer, weight decay 0.00001, learning rate 0.0001, GELU activation, sigmoid out activation, L1 loss, and a learning rate scheduler reducing by  $\times 10$  on plateaus with a patience of 100. The weights are trained from scratch and initialized with the pytorch default Kaiming uniform initialization with negative slope  $\sqrt{5}$  (He et al., 2015).

Choosing the tile size is a trade-off: we presume that a large size of input tiles enables the vanilla UNet to identify and correct large spatial biases in, e.g., the MAR inputs, increasing the accuracy. The size of the theoretical receptive field (TRF) of the chosen vanilla UNet architecture is  $(188 \times 188)\text{px}$  (see calculation below) and depends on the number of encoding blocks (here 4), kernel size, and size of the max pool. Thus, the vanilla UNet can theoretically correct biases of the MAR inputs within a radius 18.8km ( $=188\text{px} \times 100\text{m/px}$ ),

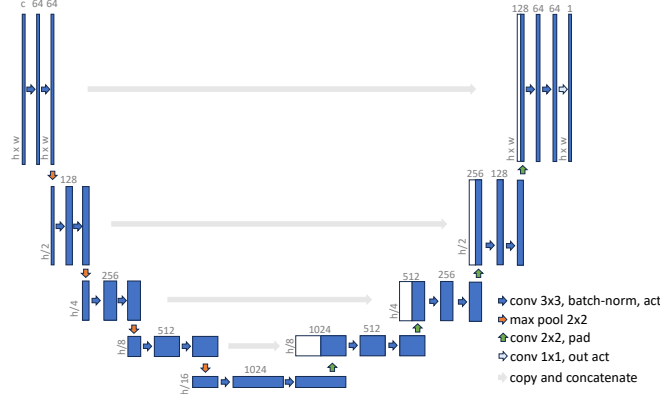


Figure B1: **Vanilla UNet architecture.** The vanilla UNet combines an encoder-decoder architecture with skip connections. The numbers beside and above the blue embedding layers represent the spatial and feature dimension, respectively. The feature dimension is constant in between layers for which the depicted layer width remains constant.

which intersects a maximum of  $(5 \times 5)$  MAR pixels of  $5km/px$  resolution. In general, the quality of CNN predictions is known to degrade towards the image borders due to the increasing influence from border padding. Given the TRF, any output pixels within 188px of the image border could theoretically contain edge artifacts. Thus, increasing the tile size also increases the number of pixels that are not affected by edge artifacts. The downside however is that larger tile size increases computational cost and can increase the required data for training (Wang et al., 2018). After initial experiments (unshown), we determined a tile size of 512 as a good trade-off.

The size of the theoretical receptive field (TRF) can be computed layerwise by starting with the center-pixel of the output and counting how many pixels in the previous layers it connects to. For the decoder, the output center-pixel connects to 4 pixels in the final  $32 \times 32 \times 1024$  feature vector. For the encoder, every  $3 \times 3$  convolution adds 2 pixels to the receptive field and every  $2 \times 2$  max pool doubles the receptive field. For example, the center-pixel connects to  $4 + 2 + 2 = 8$  pixels in the  $32 \times 32 \times 512$  feature vector; connects to  $8 * 2 + 2 + 2 = 20$  pixels in the  $64 \times 64 \times 256$  feature vector; connects to  $20 * 2 + 2 + 2 = 44$  in the  $128 \times 128 \times 128$  feature vector; ...; and connects to  $92 * 2 + 2 + 2 = 188$  pixels in the input layer which is the TRF. This calculation could also be written as  $4 * 2^b + \sum_{b'=0}^b 4 * 2^{b'}$  with  $b = \{0, 1, \dots, 4\}$  reverse-indexing the blocks. The effective receptive field is smaller than the TRF, because the number of connections per input pixel to the output center-pixel decreases with the distance from the input center-pixel (Loos et al., 2024).

## B7 Model set-up: UNet SMP

Our optimized UNet SMP has  $49,569,081 \approx 49.6M$  weights occupying 189MB at float32 precision. The model encoder is fully detailed in Sec. 3.2 and Fig. 4 (L.-C. Chen et al., 2018) as ‘modified aligned xception’, X-71. This encoder’s main component are 22x xception blocks that each contain 3x depthwise-separable convolution blocks and a skip connection. Each of the depthwise-separable convolution blocks applies a depthwise convolution, batch normalization, ReLU, pointwise convolution, batch normalization, and ReLU. Separating the convolution across the horizontal (depth) and channel (point) dimension allows for deeper networks while maintaining a similar number of parameters. The encoder reduces the spatial dimension by a factor of  $32\times$  by using convolutions with stride = 2. We do not use atrous spatial pyramid pooling in the UNet SMP encoder. The encoder is pretrained on



ImageNet-1k which is a classification task on RGB data. We initially expected that these weights would not transfer well to our multi-modal dataset (Zhu et al., 2024), but saw clear gains in the validation SSIM score in ablation experiments to randomly initialized weights. The decoder is similar to (Ronneberger et al., 2015), uses five resolution levels, and is trained from scratch.

The reported results were trained with batch size 8, tile size  $h = w = 512$ , adam optimizer, no weight decay, 18 workers, batch norm in the encoder but not in the decoder, ReLU activation, and a sigmoid activation in the output layer. Our scores improved by using a ‘CosineAnnealingWarmRestarts’ scheduler that reduces the learning rate from an initial, 0.0001, to 0. within the first cycle of  $T_0 = 35$  epochs, and resets the learning rate afterwards. We train for a total of 1085 epochs restarting this cycle  $5\times$  and increasing  $T$  by  $2\times$  after every restart (Loshchilov & Hutter, 2017). Using *GELU* marginally improved scores in the vanilla UNet, but is unavailable in the reference codebase so we use *ReLU*.

### B8 Model set-up: DeepLabv3+

Our DeepLabv3+ model is the model described in (L.-C. Chen et al., 2018), including atrous spatial pyramid pooling, and we use the implementation in segmentation models pytorch (Iakubovskii, 2023). The DeepLabv3+ model is also a CNN-based encoder-decoder architecture, but in comparison to the vanilla UNet, has 30% more parameters, only one skip connection, and a larger receptive field by using atrous convolutions with different rates in the bottleneck layer (L.-C. Chen et al., 2018). The model has 42.9M weights occupying 164MB at float32 precision.

We swept over the encoder size (tu-xception41p vs. tu-xception71), encoder output stride (8,16), learning rate (0.001,0.0001,0.00001), decoder atrous rates ([6,12,18],[12,24,36],[24,48,72]), and weight decay (0.0001,0.). Both model sizes, tu-xception41p with 28.0M and tu-xception71 with 42.9M parameters, showed similar performance while we found tu-xception71 to have slightly better SSIM and tu-xception41p with slightly better MAE, MSE, and R2. We selected the hyperparameters that achieved the highest SSIM score on the validation dataset. The reported model uses the parameters: epochs 1085 (stopped at 1081), batch size 16, tile size  $h = w = 304$ , encoder tu-xception71, initial learning rate 0.001, weight decay 0., adam optimizer, ReLU activation, sigmoid out activation, encoder depth 5, encoder output stride 8, decoder channels 256, decoder atrous rates [6, 12, 18],  $4\times$  upsampling, we use batch normalization, a cosine annealing scheduler with warm restarts and  $T_0 = 35$ ,  $T_{\text{mult}} = 2$ ,  $\eta_{\text{min}} = 0.$ , and masked L1-loss. No data augmentations were applied. The network weights are randomly initialized. To generate large-scale tifs with this model, we use a prediction stride of  $s_{\text{val}} = s_{\text{test}} = 240$ , and an erode size of  $e_{\text{val}} = e_{\text{test}} = 32$  which, paired with the 304px tile size, results in no overlap between each tile.

During the hyperparameter sweep we found that a higher learning rate, larger model, and no weight decay increased the performance. We observed no conclusive trends in varying the encoder output stride or decoder atrous rates. DeepLabv3+ was trained for 1065 epochs taking 21 hours. In preliminary experiments, we also trained the SR3 diffusion model (Saharia et al., 2023) which required significantly longer training times.

## Appendix C Additional Results

### C1 Additional metrics

Table C1 shows additional metrics for each traditional method, UNet, and DeepLabv3+. The RMSE is computed as:

$$\text{RMSE}(\mathbf{Y}, \hat{\mathbf{Y}}) = \sqrt{\text{MSE}(\mathbf{Y}, \hat{\mathbf{Y}})} \quad (\text{C1})$$

Table C1: **Results table.** Mean and standard deviation of additional evaluation metrics for each model across the test dataset. The standard deviation is computed according to Eq. (C3), best scores are **bold**, and we report three significant digits. UNet SMP is abbreviated as UNet.

Model	PSNR <sub>s</sub>	RMSE <sub>s</sub>	$R^2$	Prec.	Rec.	$\sigma_{\text{MAE}_s}$	$\sigma_{\text{MSE}_s}$	$\sigma_{\text{Acc.}}$	$\sigma_{\text{SSIM}}$
Time-interpolate SAR	14.1	0.197	0.579	0.755	<b>0.880</b>	0.0425	0.0346	0.0679	0.0878
Interpolate MAR	8.276	0.386	-0.0518	0.753	0.593	0.0902	0.084	0.0992	0.179
Threshold PMW	5.959	0.504	-0.464	0.662	0.480	0.149	0.145	0.148	0.189
Threshold DEM	8.638	0.370	0.103	0.750	0.654	0.106	0.0926	0.103	0.165
DeepLabv3+	14.8	0.182	0.648	0.846	0.815	0.0285	0.0207	0.0287	0.0812
UNet	<b>16.0</b>	<b>0.158</b>	<b>0.735</b>	<b>0.866</b>	0.831	0.0252	0.0170	0.0267	0.0747
Vanilla UNet	14.5	0.189	0.603	0.814	0.868	0.0322	0.0271	0.0319	0.0784
test-val score diff.	0.268	0.00775	0.0164	0.0117	0.0282	n/a	n/a	n/a	n/a

with the same unit as the targets (surface meltwater fraction per 100m grid cell). The PSNR is computed as:

$$\text{PSNR}(\mathbf{Y}, \hat{\mathbf{Y}}) = 10 \log_{10}(s_{\max}^2 / \text{MSE}(\mathbf{Y}, \hat{\mathbf{Y}})) \quad (\text{C2})$$

with the maximum image value  $s_{\max} = 1$ , and using decibels as the unit.

We compute the standard deviation across images for the spatial error metrics,  $\text{Err}_s$ , weighted by the amount of valid pixels in each image. This provides a measure of the error variance across images rather than across valid pixels.

$$\sigma(\mathbf{Y}, \hat{\mathbf{Y}}) = \sqrt{\frac{1}{N_{\text{valid}}} \sum_k^K n_{\text{valid},k} \left[ \frac{1}{n_{\text{valid},k}} \sum_{(i,j) \in I_{J_{\text{valid},k}}} (|y_{k,i,j} - \hat{y}_{k,i,j}|)^p - \text{Err}_s(\mathbf{Y}, \hat{\mathbf{Y}}) \right]^2} \quad (\text{C3})$$

The test-val score difference is computed by, first, computing the score for each model on the test set and on the val set. Then, we take the difference between the test and val set score for each model. Lastly, we compute the absolute value of this difference and, then, take an average across all models.

## C2 Meltwater extent per day

Figure C1 was created by training each model on the training set and then comparing each model's predictions against every available observation in the test dataset. Because of the partial masks in each SAR observation we plot the average meltwater fraction per observed pixel. Some SAR observations contain valid pixels only in a small subsection of our study area meaning large deviations of the ML models are less representative of the full study area. Thus, we mark days for which  $< 20\%$  of pixels are valid by shading the X-marker.

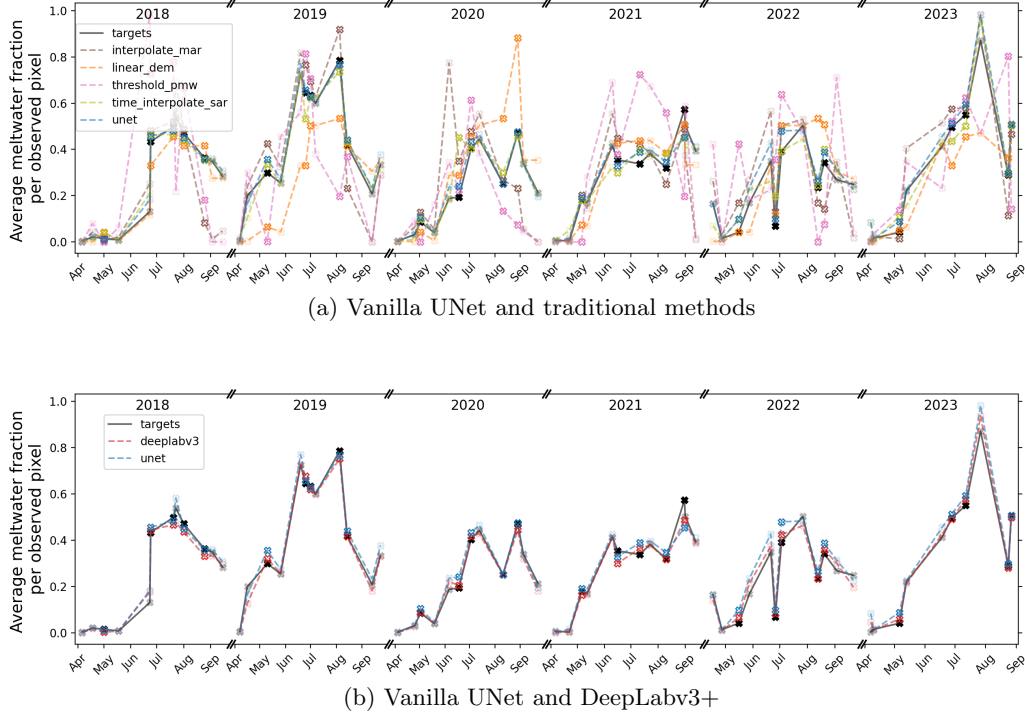


Figure C1: **Predicted and observed daily surface meltwater fraction on the test set.** The black line shows the observed surface meltwater fraction as an average across all pixels that were valid and observed on the given day. The same valid-pixel mask is applied to the predictions before plotting the surface meltwater fraction average. The X-marker is shaded on days with < 20% valid pixels and solid otherwise.

Figure C2 shows the daily predictions of total cumulative surface meltwater for the vanilla UNet and DeepLabv3+. Notably, DeepLabv3+ predicts less meltwater in comparison to the vanilla UNet which is also reflected by the better precision and worse recall in Table C1.

### C3 Deep learning hyperparameter insights

Overall the hyperparameter tuning improved the scores from  $\sim 0.715$  to  $\sim 0.765$  SSIM, but took significant effort. We varied over model architectures [UNet, DeepLabv3+], backbone families [Xception, ResNet, ConvNeXt], learning rates [1e-6 to 1e-2], batch norm, pretrained vs. randomly initialized weights, a scheduler that reduces the learning rate when the loss curve plateaus vs. a cosine annealing scheduler with warm restarts (Loshchilov & Hutter, 2017), tile size [32,64,128,256,512], activation function [ReLU, GELU], and the loss function [L1, L2]. Using batch norm stabilized our training, i.e., without batch norm some models with high learning rate ( $> 0.001$ ) diverged to poor SSIM values ( $< 0.4$ ) and activating batch norm remediated that. Using the cosine annealing scheduler slightly improved our results ( $\sim 0.01$  SSIM on a UNet with Xception71 backbone) in an ablation with the plateau scheduler. The DeepLabv3+ predictions are slightly blurry, partially due to a final 4x upsampling layer that is not followed by any additional layers. Reducing the prediction stride and increasing erode size during inference achieved only negligible improvement in SSIM ( $\sim 0.005$ ), but took significant extra compute.

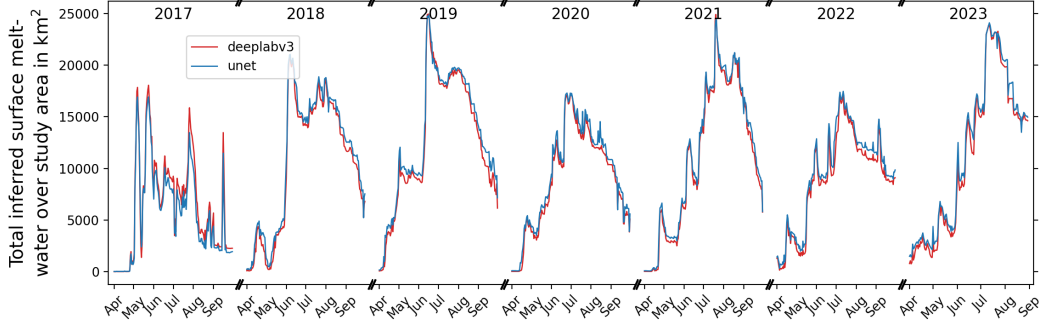


Figure C2: Predictions of total cumulative surface meltwater per day by the vanilla UNet (blue) and DeepLabv3+ (red) for every day in the study period 2017-2023.

## Appendix D Extended Discussion

The biases of the threshold DEM model likely reflect the shift in distribution between train and test dataset, visualized in Fig. 6b. In particular, we note that there is less meltwater during August in the test dataset in comparison to the training dataset and the threshold DEM model, only using static information as inputs, does not contain any information on this distribution shift.

### D1 MeltwaterBench as testbed dataset for ML algorithm development

We developed MeltwaterBench to evaluate data-driven downscaling algorithms in the context of surface meltwater. Nevertheless, the assembled benchmark might also be suitable for studying fundamental ML advances in the following areas:

**Physics-constrained ML.** Physics-informed ML downscaling methods are an active area of interest (Lütjens et al., 2024; Abraham, 2025). A common assumption in physics-informed ML downscaling is that patch-based averages of the predicted high-resolution field equal the corresponding low-resolution pixel values (Harder et al., 2023). However, this assumption is not valid between the MeltwaterBench inputs and targets, indicating that the benchmark poses novel challenges for embedding physical constraints into downscaling algorithms. An interesting physics-informed approach could be to consider surface mass balance or to split downscaling into a bias-correction and superresolution task.

**Foundation models.** Current benchmarks for geospatial foundation models do not include a downscaling task (Lacoste et al., 2023; Marsocci et al., 2024). However, geospatial foundation models could be highly applicable to the downscaling problem due to the need for data efficient models. In our case, for example, the size of the target dataset is limited by the number of retrievals during the S1A&-B SAR satellite lifetime. And, even expanding the training dataset with meltwater observations over other locations could come with a considerable domain shift, for example, due to the increasing ponding of meltwater in Western Greenland or the wind-driven freezing over Antarctica’s Larsen C Ice Shelf. Thus, geospatial foundation models that are pretrained on vast datasets to promise data-efficient fine-tuning could help (Klemmer et al., 2025; Jakubik et al., 2025), and it would be an interesting outcome if they can improve on our task-specialized UNet baseline.